

A continuous satellite-derived global record of land surface evapotranspiration from 1983 to 2006

Ke Zhang,^{1,2} John S. Kimball,^{1,2} Ramakrishna R. Nemani,³ and Steven W. Running²

Received 21 October 2009; revised 24 May 2010; accepted 1 June 2010; published 18 September 2010.

[1] We applied a satellite remote sensing–based evapotranspiration (ET) algorithm to assess global terrestrial ET from 1983 to 2006. The algorithm quantifies canopy transpiration and soil evaporation using a modified Penman–Monteith approach with biome-specific canopy conductance determined from the normalized difference vegetation index (NDVI) and quantifies open water evaporation using a Priestley–Taylor approach. These algorithms were applied globally using advanced very high resolution radiometer (AVHRR) GIMMS NDVI, NCEP/NCAR Reanalysis (NNR) daily surface meteorology, and NASA/GEWEX Surface Radiation Budget Release–3.0 solar radiation inputs. We used observations from 34 FLUXNET tower sites to parameterize an NDVI-based canopy conductance model and then validated the global ET algorithm using measurements from 48 additional, independent flux towers. Two sets of monthly ET estimates at the tower level, driven by in situ meteorological measurements and meteorology interpolated from coarse resolution NNR meteorology reanalysis, agree favorably (root mean square error (RMSE) = 13.0–15.3 mm month^{−1}; R^2 = 0.80–0.84) with observed tower fluxes from globally representative land cover types. The global ET results capture observed spatial and temporal variations at the global scale and also compare favorably (RMSE = 186.3 mm yr^{−1}; R^2 = 0.80) with ET inferred from basin-scale water balance calculations for 261 basins covering 61% of the global vegetated area. The results of this study provide a relatively long term global ET record with well-quantified accuracy for assessing ET climatologies, terrestrial water, and energy budgets and long-term water cycle changes.

Citation: Zhang, K., J. S. Kimball, R. R. Nemani, and S. W. Running (2010), A continuous satellite-derived global record of land surface evapotranspiration from 1983 to 2006, *Water Resour. Res.*, 46, W09522, doi:10.1029/2009WR008800.

1. Introduction

[2] Evapotranspiration (ET) is a major component of the global water cycle and represents a critical link between terrestrial water, carbon, and surface energy exchanges. The world has experienced persistent climatic warming attributed largely to human activities over the past century [Trenberth *et al.*, 2007], and the warming is projected to continue [Meehl *et al.*, 2007]. Recent climatic changes have altered the global water cycle and surface energy budget [Huntington, 2006; Trenberth *et al.*, 2007]. To better understand these regional and global water balance changes, each term in the terrestrial water balance equation, $\Delta s = P - ET - R$, must be accurately measured or quantified. Precipitation (P) and runoff (R) can be directly measured by in situ weather stations and stream gauge networks. However, ET is inherently difficult to measure and predict especially at large spatial scales. Recent advances in retrieval algorithms and satellite remote sensing technology now enable large-scale mapping

and monitoring of ET [e.g., Cleugh *et al.*, 2007; Fisher *et al.*, 2008; Mu *et al.*, 2007; Zhang *et al.*, 2009], P [e.g., Hong *et al.*, 2005; Hsu *et al.*, 1997; Huffman *et al.*, 2007; Joyce *et al.*, 2004; Kummerow *et al.*, 2001; Sorooshian *et al.*, 2000], and water storage (Δs) [Tapley *et al.*, 2004]. However, basin-scale water budget closure is rarely, if ever, achieved due to large and variable uncertainties and inconsistencies among the water budget terms and associated products [Pan and Wood, 2006; Sheffield *et al.*, 2009; Ferguson *et al.*, 2010]. Improved accuracy in quantifying the magnitude and variability of regional and global water and energy fluxes, closing the water budget worldwide and hence improving weather forecasting, climate, and water availability assessments are the ultimate goals of current water and energy cycle research.

[3] Remote sensing (RS), especially from polar-orbiting satellites, provides relatively frequent and spatially contiguous measurements for global monitoring of surface biophysical variables affecting ET, including albedo, vegetation type, and density. There are a multitude of RS-based ET products derived from simplified process models [e.g., Monteith, 1972; Norman *et al.*, 1995; Priestley and Taylor, 1972] driven by RS inputs [Anderson *et al.*, 2008; Cleugh *et al.*, 2007; Fisher *et al.*, 2008; Mu *et al.*, 2007], thermal RS-based surface energy balance (SEB) approaches [Bastiaanssen *et al.*, 1998; Kalma and Jupp, 1990; Su, 2002], and empirical, vegetation index–ET relationships, i.e., the triangle method or its derivatives [Gillies *et al.*,

¹Flathead Lake Biological Station, University of Montana, Polson, Montana, USA.

²Numerical Terradynamic Simulation Group, University of Montana, Missoula, Montana, USA.

³NASA Ames Research Center, Moffett Field, California, USA.

1997; Nemani and Running, 1989; Nishida et al., 2003; Q. Tang et al., 2009]. Comprehensive reviews of the historical development and accuracies of in situ and RS-based ET estimation methods are provided elsewhere [e.g., Glenn et al., 2007; Kalma et al., 2008]. The various RS-based ET methods have different spatial scales and domains, temporal coverage, input requirements, and accuracies. However, there is currently no continuous, long-term (i.e., from the early 1980s) satellite-based global ET record available for global change studies.

[4] Cleugh et al. [2007] proposed a methodology that estimates 8 day evaporation at 1 km spatial resolution using gridded meteorological fields and the Penman-Monteith (PM) equation [Monteith, 1965], where the surface conductance term is a simple function of remotely sensed leaf area index (LAI) from the Moderate Resolution Imaging Spectrometer (MODIS). Mu et al. [2007] revised the surface conductance model of Cleugh et al. [2007] to produce a global ET algorithm by accounting for stomata response to temperature and atmospheric humidity deficit and introducing a separate soil evaporation term not explicitly considered by Cleugh et al. [2007]. This algorithm was further modified by incorporating surface meteorology retrievals from AMSR-E microwave remote sensing over the high latitudes [Mu et al., 2009] and is experiencing other ongoing improvements. Meanwhile, Leuning et al. [2008] developed a biophysical, six-parameter surface conductance model, which can be reduced to a two-parameter model, driven by LAI to replace Cleugh et al.'s empirical surface conductance model. The Leuning et al. model accounts for stomatal conductance sensitivity to atmospheric humidity deficit and light, and includes a simple term for soil evaporation; the ET results derived using optimized parameters showed improved performance relative to Cleugh et al.'s model in relation to measurements from 15 global flux station sites. In a companion study, Y. Zhang et al. [2008] optimized the parameters of this model using steady state water balance estimates (P-R) from gauged catchments in Australia and applied the model to estimate catchment-level evaporation. These studies show favorable ET accuracy at both site and catchment levels [Leuning et al., 2008; Y. Zhang et al., 2008]. However, this approach is sensitive to uncertainty in LAI inputs [Leuning et al., 2008]. It is also necessary to optimize the model parameters [Y. Zhang et al., 2008]; thus, additional parameter optimization is likely to be needed for global application of this approach. The Leuning et al. and Mu et al. models are also limited by global LAI availability and accuracy in the pre-MODIS era (i.e., before 2000). Alternatively, the normalized difference vegetation index (NDVI) is sensitive to photosynthetic leaf area and calculated directly from satellite sensor spectral reflectances. Unlike the downstream LAI product, there are no model-related errors in NDVI. The NOAA advanced very high resolution radiometer (AVHRR)-based NDVI record extends from 1981 to present and can be used for global long-term ET mapping since NDVI is sensitive to vegetation structure and photosynthetic canopy cover. The results of Cleugh et al. [2007], Mu et al. [2007], and Leuning et al. [2008] show that the PM equation is a biophysically sound and robust framework for estimating daily ET at regional to global scales using remotely sensed data.

[5] We developed a biome-specific, NDVI-based canopy conductance model that accounts for stomata response to temperature and atmospheric vapor pressure deficit and the

unique physiological characteristics of different biomes [Zhang et al., 2009]. Canopy conductance is defined using empirical relationships between potential surface conductance (g_0) and NDVI and reduced by temperature and moisture constraint multipliers. The canopy conductance and NDVI functional relationships are derived for different biomes using regional flux tower measurements and then coupled with PM based canopy and soil evaporation models, and a Priestly-Taylor (PT)-based open water evaporation model to determine the aggregated ET of a grid cell. This approach was successfully applied to produce a long-term (1983–2005) daily ET record for the pan-Arctic basin and Alaska [Zhang et al., 2009]. These results showed generally improved performance over Mu et al.'s global ET method in relation to tower based meteorology from 14 sites representing regionally dominant biomes. However, the northern biomes represent less than half of all global land cover types. Moreover, NDVI and canopy conductance relationships were only defined for four regionally dominant biomes due to sparse regional tower eddy covariance measurements.

[6] In this study, we extend our RS NDVI-based ET algorithm to the global domain and derive biome specific NDVI-based canopy conductance functions for all major global biomes using surface energy fluxes and meteorology measurements from the global FLUXNET tower network [Baldocchi, 2008]. The objectives of this study are to (1) derive biome-specific NDVI-based canopy conductance functions for the major global biome types and correspondingly refine the RS NDVI-based ET algorithm for global applications and (2) generate a global long-term (1983–2006) daily ET record with well-quantified accuracy for studies on regional/global water balances changes.

2. Theory

2.1. ET Algorithm Logic

[7] We extended an NDVI-based ET algorithm developed for the northern high latitudes in the work of Zhang et al. [2009] to a global domain for this study. The core components of the ET algorithm are similar to those of Zhang et al. [2009], but with substantial algorithm modifications needed for global applications, including (1) deriving biome-specific canopy conductance versus NDVI functions for the major global biome types using daily eddy covariance and associated meteorological measurements from globally distributed tower sites, (2) replacing the calculation of soil heat flux and heat storage as a constant fraction of net radiation with more physically based equations, (3) calculating ET for mixed forest land cover types as a composite of component ET values from the distinct growth forms (e.g., deciduous versus evergreen) comprising this class rather than as a single biome type.

[8] In our ET algorithm, energy at the surface of the earth is governed by the surface energy balance equation,

$$R_n = H + \lambda E + G, \quad (1)$$

where R_n (W m^{-2}) is the net radiation flux, H (W m^{-2}) is the surface sensible heat flux, λE (W m^{-2}) is the surface latent heat flux (LE), and G is the sum of the soil heat flux and

heat storage in above-ground biomass for vegetated areas or heat storage in water bodies. R_n is calculated using

$$R_n = R_{ns} - R_{nl} = (1 - \alpha)R_{s\downarrow} - R_{nl}, \quad (2)$$

where R_{ns} is net shortwave (i.e., solar) radiation, $R_{s\downarrow}$ is incoming shortwave radiation, α is surface albedo, and R_{nl} is outgoing net longwave radiation. R_{nl} is calculated using the method of *Allen et al.* [1998],

$$R_{nl} = \sigma \left[\frac{T_{\max,K}^4 + T_{\min,K}^4}{2} \right] (0.34 - 0.14\sqrt{e_a}) \left(1.35 \frac{R_{s\downarrow}}{R_{so}} - 0.35 \right), \quad (3)$$

where σ is the Stefan-Boltzmann constant (4.903×10^{-9} MJ K⁻⁴ m⁻² d⁻¹), $T_{\max,K}$ and $T_{\min,K}$ are the daily maximum and minimum air temperature in Kelvin, respectively, e_a (Pa) is the actual daily air water vapor pressure, and R_{so} (W m⁻²) is clear-sky incoming shortwave radiation.

[9] In our algorithm, we first identified open water body and vegetated pixels using a remote sensing-derived global land cover classification. For vegetated pixels, we used the PM equation with a biome-specific NDVI-based canopy conductance model to calculate vegetation transpiration and a modified PM equation to calculate soil evaporation. We used the PT method to calculate evaporation for water body pixels.

2.1.1. Evapotranspiration for Vegetated Areas

[10] ET for vegetated areas is partitioned into soil evaporation and canopy transpiration by partitioning available energy for ET using the fractional vegetation cover (f_c) derived from satellite observed NDVI. Detailed information about f_c is available elsewhere [e.g., *Mu et al.*, 2007]. The available energy for ET (A : W m⁻²) is determined as the difference between R_n and G . For vegetated areas, G is calculated as a function of R_n and f_c according to *Su et al.* [2001],

$$G = R_n \times [\Gamma_c + (1 - f_c) \times (\Gamma_s - \Gamma_c)], \quad (4)$$

where Γ_c and Γ_s are the ratios of G to R_n for full vegetation canopy and bare soil, respectively. *Su et al.* [2001] assumed Γ_c and Γ_s as global constants, while we regarded Γ_c and Γ_s as biome-specific constants in this study.

[11] The A term is then linearly partitioned into available energy components for the canopy (A_{Canopy} : W m⁻²) and soil surface (A_{Soil} : W m⁻²) using f_c such that

$$A_{\text{Canopy}} = A \times f_c, \quad (5)$$

$$A_{\text{Soil}} = A \times (1 - f_c). \quad (6)$$

[12] The PM equation is used to calculate vegetation transpiration as

$$\lambda E_{\text{Canopy}} = \frac{\Delta A_{\text{Canopy}} + \rho C_p (e_{\text{sat}} - e_a) g_a}{\Delta + \gamma(1 + g_a/g_s)}, \quad (7)$$

where $\lambda E_{\text{Canopy}}$ (W m⁻²) is the latent heat flux of the canopy (i.e., LE_{Canopy}) and λ (J kg⁻¹) is the latent heat of vaporization; $\Delta = d(e_{\text{sat}})/dT$ (Pa K⁻¹) and is the slope of the curve relating saturated water vapor pressure (e_{sat} : Pa) to air temperature (T : K); $e_{\text{sat}} - e$ is equal to the vapor pressure

deficit (VPD: Pa); ρ (kg m⁻³) is the air density; C_p (J kg⁻¹ K⁻¹) is the specific heat capacity of air; and g_a (m s⁻¹) is the aerodynamic conductance. The psychrometric constant is given by $\gamma = (M_a / M_w)(C_p P_{\text{air}} / \lambda)$ where M_a (kg mol⁻¹), M_w (kg mol⁻¹), and P_{air} (Pa) are the molecular mass of dry air, the molecular mass of wet air, and the air pressure, respectively. The g_s (m s⁻¹) term in the original PM equation is the surface conductance. Since we use the PM equation to calculate canopy transpiration in this section, the g_s term is identical to the canopy conductance (g_c), where g_c is calculated using a biome-specific NDVI-based Jarvis-Stewart-type canopy conductance model [*Zhang et al.*, 2009],

$$g_c = g_0(\text{NDVI}) \times m(T_{\text{day}}) \times m(\text{VPD}), \quad (8)$$

where g_0 (NDVI) is the biome-dependent potential (i.e., maximum) value of g_c , which is a function of NDVI; T_{day} (°C) is the daylight average air temperature; $m(T_{\text{day}})$ is a temperature stress factor and function of T_{day} ; $m(\text{VPD})$ is a water/moisture stress factor and function of VPD. The temperature stress factor $m(T_{\text{day}})$ follows the equation detailed by *June et al.* [2004] with an optimum temperature T_{opt} ,

$$m(T_{\text{day}}) = \begin{cases} 0.01 & T_{\text{day}} \leq T_{\text{close_min}} \\ \exp\left(-\left(\frac{T_{\text{day}} - T_{\text{opt}}}{\beta}\right)^2\right) & T_{\text{close_min}} < T_{\text{day}} < T_{\text{close_max}} \\ 0.01 & T_{\text{day}} \geq T_{\text{close_max}} \end{cases}, \quad (9)$$

where T_{opt} (°C) is a biome-specific optimal air temperature for photosynthesis; $T_{\text{close_min}}$ (°C) and $T_{\text{close_max}}$ (°C) are the biome-specific minimum and maximum critical temperatures for stomatal closure and the effective cessation of plant photosynthesis; β (°C) is a biome-specific parameter and is the difference in temperature from T_{opt} at which temperature stress factor falls to 0.37 (i.e., e^{-1}). The $m(\text{VPD})$ term is calculated as,

$$m(\text{VPD}) = \begin{cases} 1.0 & \text{VPD} \leq \text{VPD}_{\text{open}} \\ \frac{\text{VPD}_{\text{close}} - \text{VPD}}{\text{VPD}_{\text{close}} - \text{VPD}_{\text{open}}} & \text{VPD}_{\text{open}} < \text{VPD} < \text{VPD}_{\text{close}} \\ 0.1 & \text{VPD} \geq \text{VPD}_{\text{close}} \end{cases}, \quad (10)$$

where VPD_{open} (Pa) is the biome-specific critical value of VPD at which the canopy stomata are completely open; $\text{VPD}_{\text{close}}$ (Pa) is the biome-specific critical value of VPD at which canopy stomata are completely closed.

[13] Soil evaporation is calculated using the soil evaporation equation from *Mu et al.* [2007] and *Zhang et al.* [2009], which is a combination of an adjusted PM equation and the complementary relationship hypothesis [*Bouchet*, 1963; *Fisher et al.*, 2008]. The soil evaporation equation and its auxiliary equations include,

$$\lambda E_{\text{Soil}} = \text{RH}^{(\text{VPD}/k)} \frac{\Delta A_{\text{Soil}} + \rho C_p \text{VPD} g_a}{\Delta + \gamma \times g_a / g_{\text{totc}}}, \quad (11)$$

$$g_a = g_{ch} + g_{rh}, \quad (12)$$

$$g_{rh} = (4.0 \times \sigma \times T_{day}^3) / (\rho C_p), \quad (13)$$

$$g_{totc} = g_{tot} \times G_{corr}, \quad (14)$$

$$G_{corr} = \left(\frac{273.15 + T_{day}}{293.15} \right) \times \frac{101300}{P_{air}}, \quad (15)$$

where RH is the relative humidity of air with values between 0 and 1; $RH^{(VPD/k)}$ is a moisture constraint on soil evaporation [Fisher *et al.*, 2008], which is an index of soil water deficit based on the complementary relationship of Bouchet [1963] whereby surface moisture status is linked to and reflects the evaporative demand of the atmosphere. The assumption is that soil moisture is reflected in the adjacent atmospheric moisture. k (Pa) is a parameter to fit the complementary relationship and reflects the relative sensitivity to VPD [Fisher *et al.*, 2008]. In this study, considering the possible impacts of different vegetation morphology and root zone structure among different biomes on this complementary relationship, we empirically adjusted the k parameter for different vegetation types. The g_{rh} ($m s^{-1}$) term is the conductance to radiative heat transfer and is calculated using equation (13) following Choudhury and DiGirolamo [1998]. In equation (13), T_{day} is in Kelvin. The g_{ch} ($m s^{-1}$) term is the conductance to convective heat transfer and is assumed to be equal to the boundary layer conductance (g_{bl} : $m s^{-1}$) [Thornton, 1998]. In this study, we assigned the g_{ch} and g_{bl} terms as biome-specific constants by following Thornton [1998] and Mu *et al.* [2007]. The g_{tot} ($m s^{-1}$) term is the total aerodynamic conductance to vapor transport and the combination of surface and aerodynamic conductance components. The g_{totc} ($m s^{-1}$) term is the corrected value of g_{tot} from the standard conditions for temperature and pressure (STP) using the correction coefficient (G_{corr}) following Jones [1992]. In this study, g_{tot} is adjusted by land cover class following Zhang *et al.* [2009].

[14] The mixed deciduous and evergreen forest (MF) land cover class represents approximately 7% of the global vegetated land area as defined by a global 500 m resolution land cover map [Friedl *et al.*, 2010]. For this study, deciduous and evergreen components of the MF class were distinguished for the ET calculation. We first derived the relative proportions of each forest type within MF pixels using available satellite remote sensing-derived percentage of tree cover products representing leaf longevity (evergreen and deciduous) and leaf type (broadleaf and needleleaf) components [DeFries *et al.*, 2000a, 2000b]. We then used the above canopy transpiration and soil evaporation algorithms to calculate ET for each forest type and weighted the results to produce composite ET values for each MF pixel.

2.1.2. Evaporation Over Water Bodies

[15] For water bodies, G is calculated as a function of air temperature and effective water depth (ΔZ : m) for heat exchange, based on the premise that water surface temperature generally follows air temperature [e.g., Pilgrim *et al.*, 1998; Livingstone and Dokulil, 2001; Morrill *et al.*, 2005],

$$G = \rho_w \times c_w \times K \times (T_{avg,i} - T_{avg,i-1}) \times \Delta Z, \quad (16)$$

where ρ_w ($1.0 \times 10^3 \text{ kg m}^{-3}$) is the water density; c_w ($4.186 \text{ J g}^{-1} \text{ }^\circ\text{C}^{-1}$) is the specific heat of water; $T_{avg,i}$ and $T_{avg,i-1}$ are the daily average air temperatures for the current day and previous day, respectively; and K is the slope of the simple linear regression of water surface temperature on air temperature and represents the ratio of water temperature change to surface air temperature change. Pilgrim *et al.* [1998] reported a slope of 0.82 for the linear relationship between water temperature records and associated air temperature records in 39 Minnesota stream temperature monitoring stations. Morrill *et al.* [2005] examined the air temperature/stream water temperature relationship at a geographically diverse set of streams and found that the majority of streams showed a slope of 0.6–0.8 for the linear regression between stream temperature and air temperature. Therefore, we set K to the mean (0.7) of previously reported values. The effective water depth is the uppermost well-mixed layer of the epilimnion and depends on morphology of open water bodies and other climatic factors. The literature suggests that the depth of epilimnion varies from tens of centimeters to several meters [e.g., Mazumder *et al.*, 1990]. To simplify, we set the value of ΔZ to 1.5 m in this study.

[16] The evaporation for open water pixels was then calculated using the PT equation [Priestley and Taylor, 1972],

$$\lambda E_{\text{Water}} = a \frac{\Delta A}{\Delta + \gamma}, \quad (17)$$

where the PT coefficient a accounts for evaporation arising from the atmospheric vapor pressure deficit in addition to the equilibrium term and is set to 1.26 following Priestley and Taylor [1972]. The PT coefficient of 1.26 is generally valid for the saturated surface [Priestley and Taylor, 1972] and is even valid for wet meadow [Stewart and Rouse, 1977] and well-watered grass [Lhomme, 1997]. Therefore, we adopted this approach to estimate evaporation for smaller (length scales less than 8km) water bodies.

2.2. Biome-Specific Potential Canopy Conductance Versus NDVI Functions

[17] We used measured energy fluxes and daily meteorology from eddy covariance flux towers (see section 3) with corresponding NDVI time series from the AVHRR GIMMS data set [Pinzon *et al.*, 2005; Tucker *et al.*, 2005] to establish biome-specific relationships between g_0 and NDVI. We first removed the calculated soil latent heat flux (LE_{Soil} or λE_{Soil}) (method introduced in section 2.1.1) driven by in situ tower meteorology from the tower LE measurements to determine canopy latent heat flux (LE_{Canopy} or $\lambda E_{\text{Canopy}}$). We then derived the canopy conductance term (g_c) from LE_{Canopy} and the in situ tower meteorology using the rearranged PM equation,

$$g_c = \frac{g_a \gamma LE_{\text{Canopy}}}{\Delta A_{\text{Canopy}} + \rho C_p VPD g_a - LE_{\text{Canopy}} (\Delta + \gamma)}. \quad (18)$$

[18] Because of lack of available vertical wind profile measurements, we set values of g_a as biome-specific constants based on evidence that the range of g_a variability is generally conservative over low wind speeds (e.g., $\leq 5 \text{ m s}^{-1}$)

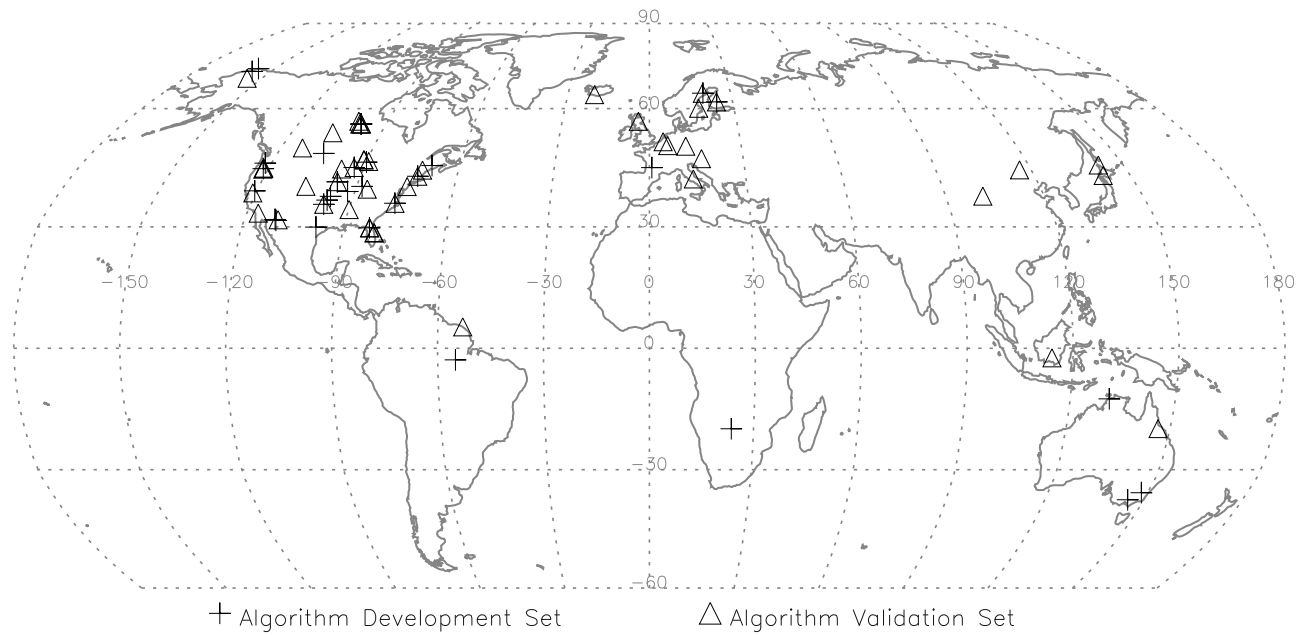


Figure 1. Locations of the flux tower sites used for ET algorithm development (34 sites) and validation (48 sites).

and aerodynamically rough surfaces following *Monteith and Unsworth* [2007]. Although the use of a constant g_a can introduce uncertainty into the ET estimates, this simplification has been successfully applied for similar satellite based ET mapping studies [e.g., *Mu et al.*, 2007; *Y. Zhang et al.*, 2008; *Zhang et al.*, 2009]. By substituting g_c in equation (18) for g_0 in equation (8) and rearranging the equation, we derived the potential surface conductance as

$$g_0 = \frac{g_a \gamma LE_{\text{Canopy}}}{[\Delta A_{\text{Canopy}} + \rho C_p VPD g_a - LE_{\text{Canopy}} (\Delta + \gamma)] \cdot m(T_{\text{day}}) \cdot m(VPD)} \quad (19)$$

[19] We (1) calculated daily g_0 for the major global biome types using daily surface meteorology and LE measurements from selected representative flux towers within each biome; (2) sorted the g_0 series for each NDVI interval (interval size = 0.04) in numeric order and removed outliers falling below the 10th percentile and above the 90th percentile for g_0 ; (3) calculated average daily values of g_0 and NDVI for each NDVI interval with sufficient (≥ 10) samples; and (4) fitted the scatter plots of g_0 versus NDVI using sigmoid response functions for each biome type following *Zhang et al.* [2009],

$$g_0(\text{NDVI}) = 1/[b_1 + b_2 \times \exp(-b_3 \times \text{NDVI})] + b_4, \quad (20)$$

where b_1 (s m^{-1}), b_2 (s m^{-1}), b_3 (dimensionless), and b_4 (m s^{-1}) are empirical parameters. Considering the constraint $g_0(0) = 0$, the b_4 parameter is equal to $-1/(b_1 + b_2)$. To analyze the uncertainty in the fitted relationship of g_0 versus NDVI, we applied an adaptive Markov chain Monte Carlo (MCMC) method [*Haario et al.*, 2006] with a chain of length 6000 to produce the 99% posterior distribution of the fitted relationship of g_0 versus NDVI for each biome type.

2.3. Global Implementation of the ET Algorithm

[20] We applied the above ET algorithm with parameterized, biome-specific NDVI-derived canopy conductance models to calculate global ET at the pixel level. We chose the 8 km resolution of the GIMMS NDVI product as the final resolution of the global ET calculations. To adequately consider land cover heterogeneity within the 8 km grid cells, we calculated the fractional coverage of every vegetation type and open water body within each 8 km grid cell using the 500 m MODIS-IGBP Collection 5 global land cover product [*Friedl et al.*, 2010] and applied the above ET algorithm to calculate ET for every vegetation and open water class within each grid cell. Finally, we used the land cover fractions as weights to sum the ET values of each land cover type within the 8 km grid cell to produce the 8 km area-average ET.

3. Data and Methods

3.1. Eddy Covariance Flux Towers

[21] We utilized tower eddy covariance and meteorological data from 82 tower sites of the FLUXNET data archive (<http://www.fluxnet.ornl.gov/>); these sites were split into separate algorithm development and parameterization (34 towers) and validation (48 towers) data sets representing the major global biome types (Figure 1). The flux tower site information is summarized in Tables 1 and 2. These sites are distributed across the world in all continents and global vegetation types (Figure 1 and Tables 1 and 2). The tower sites represent 10 of the 12 IGBP global vegetation types, including evergreen needleleaf forest (ENF), evergreen broadleaf forest (EBF), deciduous broadleaf forest (DBF), mixed forest (MF), closed shrubland (CSH), open shrubland (OSH), grassland (GRS), cropland (CRP), woody savanna (WSV), and savanna (SV). Considering the geographically wide distribution of the ENF biome type and the impacts of

Table 1. Details of the 34 FLUXNET Tower Sites Used for Deriving Biome-Specific NDVI-Based Canopy Conductance Functions for Representative Global Biome Types^a

LC	Site Abbr.	Years	Latitude	Longitude	Country	References
BENF (8 sites)	FIHYY	1996–2000	61.85	24.28	Finland	<i>Suni et al.</i> [2003]
	SWFLA	1996–1998	64.23	19.77	Sweden	<i>Lindroth</i> [2000a]
	CANS2	2001–2005	55.91	−98.52	Canada	<i>Litvak et al.</i> [2003]
	CANS4	2002–2004	55.91	−98.38	Canada	<i>Litvak et al.</i> [2003]
	CANS5	2001–2005	55.86	−98.49	Canada	<i>Litvak et al.</i> [2003]
	CAOBS	1994–2006	55.88	−98.48	Canada	<i>Dunn and Wofsy</i> [2006]
	USHO1	1996–2004	45.20	−68.74	USA	<i>Hollinger et al.</i> [2004]
	USWRC	1998–2006	45.82	−121.95	USA	<i>Falk et al.</i> [2008]
TENF (4 sites)	USSP2	1998–2004	29.76	−82.24	USA	<i>Powell et al.</i> [2008]
	USNC1	2004–2006	35.81	−76.71	USA	<i>DeForest et al.</i> [2006]
	USBLO	1999–2006	38.90	−120.63	USA	<i>Goldstein et al.</i> [2000]
	USME5	2000–2002	44.44	−121.57	USA	<i>Irvine et al.</i> [2007]
EBF (3 sites)	BRSA1	2002–2005	−2.86	−54.96	Brazil	<i>Hutyra et al.</i> [2007]
	AUTUM	2001–2006	−35.66	148.15	Australia	<i>Leuning et al.</i> [2005]
DBF (2 sites)	AUWAC	2005–2006	−37.43	145.19	Australia	<i>Wood et al.</i> [2008]
	USHA1	1992–2006	42.54	−72.17	USA	<i>Urbanski et al.</i> [2007]
CSH (1 site)	USMOZ	2004–2006	38.74	−92.20	USA	<i>Gu et al.</i> [2007]
	USLOS	2000–2006	46.08	−89.98	USA	<i>Cook et al.</i> [2004]
OSH (2 sites)	USATQ	1999–2006	70.47	−157.41	USA	<i>Kwon et al.</i> [2006]
	USBRW	1999–2001	71.32	−156.63	USA	<i>Oechel et al.</i> [2000]
WSV (2 sites)	USSRM	2004–2006	31.82	−110.87	USA	<i>Scott</i> [2010]
	AUHOW	2001–2006	−12.50	131.15	Australia	<i>Beringer et al.</i> [2007]
SV (2 sites)	USFR2	2004–2006	29.95	−98.00	USA	<i>Heinsch et al.</i> [2004]
	BOMAU	1999–2001	−19.92	23.59	Botswana	<i>Veenendaal et al.</i> [2004]
GRS (4 sites)	USARB	2005–2006	35.55	−98.04	USA	<i>Fischer et al.</i> [2007]
	USAUD	2002–2006	31.59	−110.51	USA	<i>Wilson and Myers</i> [2007]
	USFPE	2000–2006	48.31	−105.10	USA	<i>Wylie et al.</i> [2007]
	USWLR	2001–2004	37.52	−96.86	USA	<i>Coulter et al.</i> [2006]
CRP (6 sites)	FRBOR	1996–1998	44.70	0.77	France	<i>Berbigier and Lousteau</i> [2000]
	USARM	2003–2006	36.61	−97.49	USA	<i>Fischer et al.</i> [2007]
	USBO1	1996–2006	40.01	−88.29	USA	<i>Meyers and Hollinger</i> [2004]
	USNE1	2001–2006	41.17	−96.48	USA	<i>Suyker and Verma</i> [2008]
	USNE2	2001–2006	41.16	−96.47	USA	<i>Suyker and Verma</i> [2009]
	USRO3	2004–2006	44.72	−93.09	USA	<i>Griffis et al.</i> [2007]

^aThe land cover classification includes boreal and temperate evergreen needleleaf forest (BENF and TENF), evergreen broadleaf forest (EBF), deciduous broadleaf forest (DBF), mixed forest (MF), closed shrubland (CSH), open shrubland (OSH), woody savanna (WSV), savanna (SV), grassland (GRS), and cropland (CRP) vegetation types.

different climate zones on leaf longevity and associated biophysical functioning [Kikuzawa, 1995; Reich et al., 2007], we stratified the global ENF category into temperate ENF (TENF) and boreal/cold ENF (BENF) types according to a multiyear average of frost-free days ($T_{\text{Frost-free}}$: days). Frost-free days are defined as those days with above-zero (°C) daily minimum air temperature and are calculated from the NCEP/NCAR Reanalysis (NNR) surface meteorology. The ENF pixels are classified as TENF when $T_{\text{Frost-free}}$ exceeds 7 months (212 days); otherwise, the ENF pixels are classified as BENF.

[22] The following criteria were used to select flux tower sites for this study in order of decreasing importance: (1) at least two sites must be available for each vegetation type; (2) the selected sites should have data covering at least two growing seasons; and (3) the vegetation types within the tower footprints must be the same as the dominant vegetation type of the overlying 8 km resolution grid cell. The 82 tower sites were divided into two data sets representing an algorithm development set with 34 sites and an algorithm validation set with 48 sites. The algorithm development set was used to derive the biome-specific NDVI-based canopy conductance functions, while the validation set was used for independent validation of the global ET algorithm.

3.2. Satellite and Meteorological Inputs

[23] In this study, the satellite-based data inputs to the global ET algorithm include NDVI, land cover, tree cover continuous fields, and short-wave radiation terms, while the remaining daily surface meteorology inputs were obtained from the global NNR product [Kalnay et al., 1996; Kistler et al., 2001]. We derived a daily NDVI series for each 8 km pixel using temporal linear interpolation of adjacent semi-monthly values of the 8 km semimonthly AVHRR GIMMS NDVI product [Pinzon et al., 2005; Tucker et al., 2005]. The daily linear interpolation approach is a relatively simple, but effective, means for producing daily time series of satellite-observed vegetation state variables including fraction of photosynthetically active radiation (FPAR) and LAI and has been successfully applied for vegetation based analyses of the AVHRR series [e.g., Kimball et al., 2006, 2007; Zhang et al., 2007].

[24] The 500 m NASA MODIS Collection 5 IGBP global land cover classification (henceforth abbreviated as the 500 m MODIS-IGBP land cover) [Friedl et al., 2010] was used to determine the dominant land cover and fractional vegetation type within each 8 km AVHRR GIMMS grid cell. We then used the 1 km AVHRR Tree Cover Continuous Fields data [DeFries et al., 2000a, 2000b] to derive forest type (i.e., evergreen or deciduous) fractional cover of 8 km

Table 2. Details of the 48 FLUXNET Tower Sites Used for Independent Validation of the ET Algorithm Results

LC	Site Abbr.	Years	Latitude	Longitude	Country	References
BENF (12 sites)	SWDeg	2001–2005	64.19	19.57	Sweden	<i>Sagerfors et al.</i> [2008]
	ICGun	1996–1998	63.83	–20.22	Iceland	<i>Thorgeirsson and Gudmudson</i> [2000]
	FISii	2004–2005	61.83	24.19	Finland	<i>Suni et al.</i> [2003]
	UKAbe	1997–1999	56.62	–3.80	UK	<i>Clement et al.</i> [2003]
	CANS1	2002–2005	55.88	–98.48	Canada	<i>Litvak et al.</i> [2003]
	CANS3	2001–2005	55.91	–98.38	Canada	<i>Litvak et al.</i> [2003]
	CANS7	2002–2005	56.64	–99.95	Canada	<i>Litvak et al.</i> [2003]
	CANS6	2001–2005	55.91	–98.96	Canada	<i>Litvak et al.</i> [2003]
	BEBra	1996–1999	51.30	4.52	Belgium	<i>Ceulemans</i> [2000]
	GEBy	1996–1999	50.15	11.87	Germany	<i>Tenhunen and Schulze</i> [2000]
	USWi4	2002–2005	46.74	–91.17	USA	<i>Noormets et al.</i> [2007]
	USWi9	2004–2005	46.62	–91.08	USA	<i>Noormets et al.</i> [2007]
TENF (8 sites)	USMe1	2004–2005	44.58	–121.50	USA	<i>Irvine et al.</i> [2007]
	USMe2	2002–2006	44.45	–121.56	USA	<i>Irvine et al.</i> [2007]
	USMe3	2004–2005	44.32	–121.61	USA	<i>Irvine et al.</i> [2007]
	USNR1	1998–2006	40.03	–105.55	USA	<i>Monson et al.</i> [2005]
	USNC2	2004–2006	35.80	–76.67	USA	<i>DeForest et al.</i> [2006]
	USSP1	2001–2003	29.74	–82.22	USA	<i>Powell et al.</i> [2008]
	USSP3	1999–2004	29.75	–82.16	USA	<i>Powell et al.</i> [2008]
	USKS1	2002–2003	28.46	–80.67	USA	<i>Dijkstra et al.</i> [2002]
EBF (3 sites)	GUGUY	2004–2006	5.28	–52.93	French Guiana	<i>Bonal et al.</i> [2008]
	USKS2	2000–2006	28.61	–80.67	USA	<i>Dijkstra et al.</i> [2002]
	INPal	2002–2003	–2.35	114.04	Indonesia	<i>Hirano et al.</i> [2007]
DBF (1 site)	USMMS	1999–2006	39.32	–86.41	USA	<i>Schmid et al.</i> [2000]
MF (10 sites)	SWNor	1996–1998	60.08	17.47	Sweden	<i>Lindroth</i> [2000b]
	CAOAS	2002–2004	53.63	–106.20	Canada	<i>Barr et al.</i> [2006]
	BEVie	1996–1998	50.30	6.00	Belgium	<i>Aubinet et al.</i> [2001]
	USSyv	2001–2003	46.24	–89.35	USA	<i>J. Tang et al.</i> [2009]
	JATes	2001–2005	45.35	142.09	Japan	<i>Takagi et al.</i> [2009]
	USBar	2004–2006	44.06	–71.29	USA	<i>Jenkins et al.</i> [2007]
	JATom	2001–2003	42.74	141.52	Japan	<i>Kobayashi et al.</i> [2007]
	USLPH	2002–2005	42.54	–72.18	USA	<i>Hadley et al.</i> [2008]
	ITCol	1996–1997	41.87	13.63	Italy	<i>Valentini</i> [2000]
	USDix	2005–2006	39.97	–74.43	USA	<i>Clark et al.</i> [2010]
	USSO2	1997–1999	33.37	–116.62	USA	<i>Lipson et al.</i> [2005]
	OSIvo	2003–2006	68.49	–155.75	USA	<i>Epstein et al.</i> [2004]
	USVar	2000–2006	38.41	–120.95	USA	<i>Ryu et al.</i> [2008]
	AUVir	2001–2003	–19.88	146.55	Australia	<i>Leuning et al.</i> [2005]
GRS (7 sites)	CALTH	2002–2004	49.71	–112.94	Canada	<i>Wever et al.</i> [2002]
	USBkg	2004–2006	44.35	–96.84	USA	<i>Gilmanov et al.</i> [2005]
	CHXil	2003–2006	44.13	116.33	China	<i>Yuan et al.</i> [2007]
	CHHai	2002–2004	37.60	101.30	China	<i>Zhao et al.</i> [2007]
	USARc	2005–2006	35.55	–98.04	USA	<i>Fischer et al.</i> [2007]
	USGoo	2002–2006	34.25	–89.87	USA	<i>Gilmanov et al.</i> [2005]
	USWkg	2004–2006	31.74	–109.94	USA	<i>Scott</i> [2010]
	HUHeg	1997–2005	46.96	16.65	Hungary	<i>Barcza et al.</i> [2009]
CRP (3 sites)	USRo1	2004–2006	44.71	–93.09	USA	<i>Baker et al.</i> [2007]
	USNe3	2001–2006	41.18	–96.44	USA	<i>Suyker and Verma</i> [2009]

grid cells containing MF pixels distinguished by the 500 m MODIS-IGBP land cover classification.

[25] The daily net, incoming, and clear-sky incoming shortwave solar radiation terms (R_{ns} , $R_{s\downarrow}$, and R_{so}) were derived from the NASA World Climate Research Programme/Global Energy and Water-Cycle Experiment (WCRP/GEWEX) Surface Radiation Budget (SRB) Release –3.0 data sets with $1.0^\circ \times 1.0^\circ$ resolution using the Pinker/Laszlo shortwave algorithm [Pinker and Laszlo, 1992]. Daily meteorological data including maximum, minimum, and average air temperatures (T_{max} , T_{min} , and T_{avg} ; $^\circ\text{C}$) and air water vapor pressure (e_a ; Pa) were derived from the National Centers for Environmental Prediction–National Center for Atmospheric Research (NCEP–NCAR) Reanalysis (NNR) [Kalnay et al., 1996; Kistler et al., 2001]. The T_{max} , T_{min} , and T_{avg} variables were also used to calculate T_{day} and VPD. In addition, 1 km resolution USGS Global 30 Arc-Second (GTOPO30) DEM (<http://eros.usgs.gov/>

products/elevation/gtopo30/gtopo30.html) information was used to calculate pixel-wise atmospheric pressure with corrections for deviations from STP (e.g., equation (15)) and to analyze topographic complexities around the 82 flux towers. The relatively coarse NASA SRB radiation and NNR meteorology data were interpolated to the 8 km resolution ET modeling grid and 1 km tower footprint spatial scales for the ET/LE estimates using bilinear interpolation.

3.3. Evaluation of ET Algorithm Performance

[26] To evaluate ET algorithm performance, we produced two sets of LE/ET estimates at the tower level using our ET algorithm. The two sets of estimates were derived from respective tower measured and reanalysis meteorology inputs spatially interpolated to the 1 km tower locations. We then compared the two sets of LE/ET estimates with measured values from the eddy covariance flux towers at daily and

monthly time scales. This process ensured that the tower level LE/ET results represented the dominant land cover class of the local tower footprint rather than the composite regional land cover attributes of the overlying 8 km resolution grid cell of the global LE/ET database. Previous research [e.g., *K. Zhang et al.*, 2008] has shown that coarse NNR meteorology reanalysis can introduce considerable uncertainty in capturing local micrometeorology in some regions. We compared the two sets of model simulations to attribute LE/ET uncertainties between model logic error and errors due to the coarse scale reanalysis meteorology relative to tower observations. The final 8 km global LE/ET estimates are the composite values of every vegetation type and open water body delineated by the 500 m MODIS-IGBP land cover product within each 8 km grid cell. The tower-level LE/ET estimates driven by the NNR reanalysis are actually components of the final 8 km composite LE/ET falling over the tower footprints; thus, the validation of the tower-level estimates also serve as validation of the final 8 km LE/ET results. Three statistical variables were used to quantify algorithm performance, including mean residual difference (MR), root mean square error (RMSE), and simple correlation coefficient (r) between model estimates and tower measurements. The residuals are defined as the “true” values, namely, tower measurements minus model estimates. The MR is the mean value of the residuals and provides a way to quantify the bias of the estimates relative to the measurements, while the RMSE is used to describe the accuracy of the estimations. The r parameter is used to evaluate the strength of the relationships between the model results and tower observations.

[27] We verified the final global 8 km resolution ET calculations at the river basin level by comparing the model results with alternative ET estimates inferred from the long-term water balance: $\Delta s = P - ET - R$. For periods of 5 years or more, the average change in basin water storage is negligible compared to precipitation, evaporation, and runoff [e.g., *Hobbins et al.*, 2001]. Given the condition of $\overline{\Delta s} = 0$, the multiyear average water balance can be written as $ET = \overline{P} - \overline{R}$. We denoted \overline{ET} as ET_{Inferred} and the multiyear average basin-scale ET derived from the remote sensing ET products as ET_{RS} in this study. We chose 261 major global basins with relatively good records of stream flow discharge and precipitation to conduct the comparison. These basins cover 61% of global vegetated area, vary in drainage area from thousands to millions of square kilometers, and span the major global climate and vegetation zones. The observed stream flow data were compiled and provided by *Dai et al.* [2009]. The ET_{RS} and ET_{Inferred} variables were compared for the same periods between 1983 and 2006 that vary with the discharge data availability of each basin. The precipitation data were obtained from the Global Precipitation Climatology Center (GPCC) monthly precipitation database [*Rudolf and Schneider*, 2005]. The GPCC precipitation data are provided at 0.5° resolution and produced from surface gauge network observations. The GPCC precipitation data were interpolated to the 8 km resolution ET modeling grid for basin-level water balance estimates using bilinear interpolation.

3.4. Uncertainty in Reanalysis Meteorology Inputs and Impacts on LE Estimation

[28] We used the root mean squared deviation (RMSD) metric to quantify differences between interpolated NNR

and NASA/GEWEX SRB meteorology at the site level and tower-measured meteorology and between tower-driven and reanalysis-driven daily LE estimates. The RMSD statistic is defined as

$$\text{RMSD} = \sqrt{\frac{1}{n} \sum_{i=1}^n (x_{1,i} - x_{2,i})^2}, \quad (21)$$

where n is the sample size; $x_{1,i}$ is the measured value or measurement-driven estimate; and $x_{2,i}$ is the reanalysis value or reanalysis-driven estimate.

[29] We first evaluated overall accuracies of the five major meteorological variables used to drive our ET algorithm from NNR meteorology and NASA/GEWEX SRB based net radiation inputs, including T_{max} , T_{avg} , T_{min} , VPD and R_n , in relation to available daily tower measurements from all tower sites. We then analyzed the impacts of uncertainties in these variables from the NNR meteorology and NASA/GEWEX SRB solar radiation on the accuracies of reanalysis-driven daily LE estimates relative to corresponding tower-driven daily LE estimates. The RMSD values for the five variables (i.e., $\text{RMSD}(T_{\text{max}})$, $\text{RMSD}(T_{\text{avg}})$, $\text{RMSD}(T_{\text{min}})$, $\text{RMSD}(\text{VPD})$, and $\text{RMSD}(R_n)$) at the 82 tower sites were calculated. The RMSD between the tower-driven and reanalysis-driven daily LE estimates ($\text{RMSD}(\text{LE})$) were also calculated. The correlations of $\text{RMSD}(\text{LE})$ versus $\text{RMSD}(T_{\text{max}})$, $\text{RMSD}(T_{\text{avg}})$, $\text{RMSD}(T_{\text{min}})$, $\text{RMSD}(\text{VPD})$ and $\text{RMSD}(R_n)$ were then used to analyze the impacts of meteorology reanalysis uncertainties on the LE estimates.

[30] Finally, we calculated the standard deviation of DEM elevations within 100 km × 100 km windows centered over each of the 82 flux tower sites as a measure of topographic heterogeneity surrounding individual tower sites. We then compared these results with the RMSDs of the meteorological variables at the 82 sites to assess relations between topographic heterogeneity and the accuracy of NNR meteorology and NASA/GEWEX SRB solar radiation in representing local tower conditions.

4. Results

4.1. Retrieved Biome-Specific Potential Canopy Conductance Versus NDVI Functions

[31] Values of g_0 derived from tower measured surface energy fluxes and meteorology from the 34 algorithm development sites are plotted in Figure 2 against satellite-observed NDVI values of pixels overlapping the respective tower footprints for the 10 global biome types, including the TENF and BENF land cover subgroups. For all biome types, g_0 generally follows a sigmoid response curve with increasing NDVI that gradually levels off at higher NDVI values. The derived empirical parameters for the biome-specific g_0 versus NDVI relationships and other parameters used are listed in Table 3. The NDVI is an effective surrogate for canopy density. The reduced slope of this relationship at higher NDVI levels reflects increasing shading of individual leaves and leaf boundary layer adjustments with increasing canopy density. Higher canopy density can increase leaf boundary layer thickness and correspondingly reduce leaf boundary layer and canopy conductance relative to lower canopy density under the same meteorological

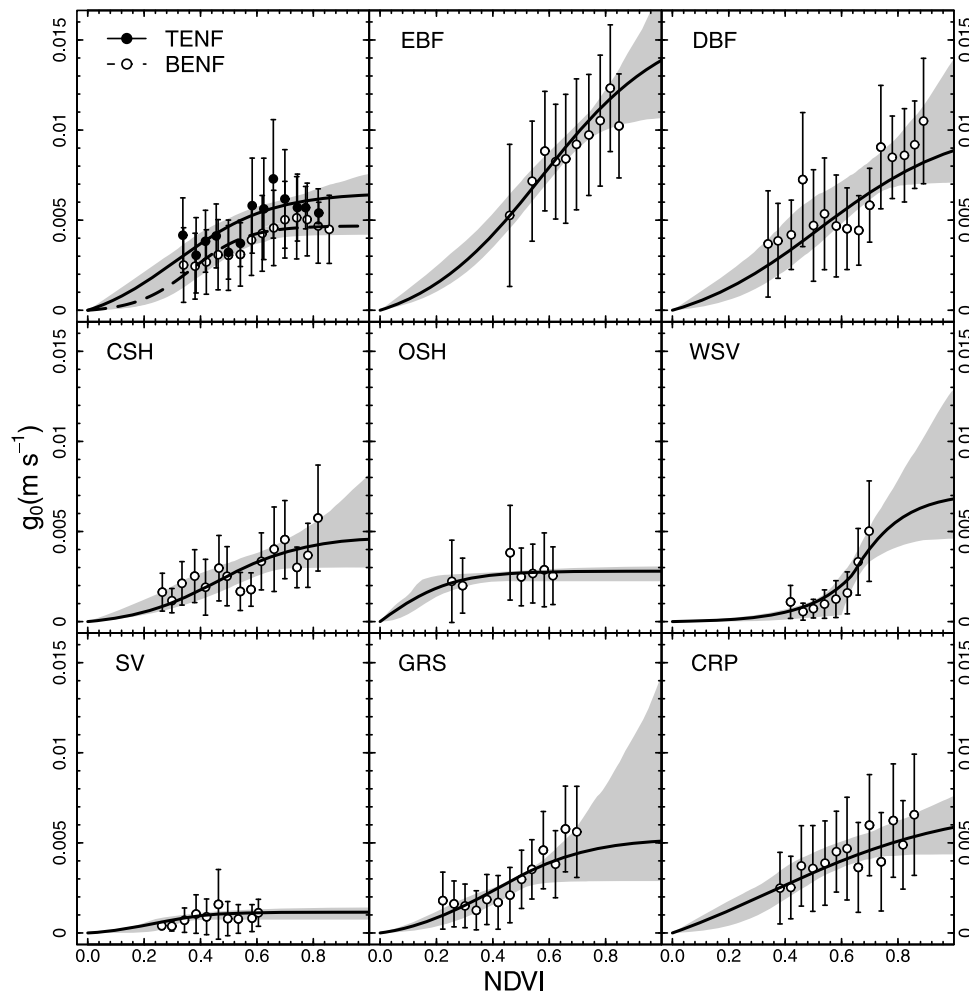


Figure 2. Scatter plots of calculated average potential surface conductance values derived from tower measurements (g_0) versus corresponding NDVI values from the AVHRR GIMMS data set and empirical fitted relationships between g_0 and NDVI using sigmoid functions for TENF, BENF, EBF, DBF, CSH, OSH, WSV, SV, GRS, and CRP vegetation types. Error bars denote the standard deviations of g_0 . Gray areas correspond to the 99% posterior limits of the fitting model uncertainty derived from an adaptive MCMC method [Haario *et al.*, 2006].

Table 3. The Biome Properties Look-up Table (BPLUT) Used for the NDVI-Based Global ET Algorithms

Parameters	BENF	TENF	EBF	DBF	CSH	OSH	WSV	SV	GRS	CRP	Sources
$T_{\text{close_min}}$ (°C)	−8	−8	−8	−6	−8	−8	−8	−8	−8	−8	1,2
$T_{\text{open_max}}$ (°C)	40	40	50	45	45	40	50	40	40	45	3,4
$\text{VPD}_{\text{close}}$ (Pa)	2800	2800	4000	2800	3300	3700	3200	5000	3800	3800	1,2,3
VPD_{open} (Pa)	500	500	500	650	500	500	500	650	650	650	1,2,3
T_{opt} (°C)	12	25	40	28	19	10	32	32	20	20	3,4
β (°C)	25	25	40	25	20	30	28	30	30	30	3
k (Pa)	150	200	300	200	400	50	900	800	500	450	3
g_a (m s ^{−1})	0.03	0.03	0.03	0.04	0.01	0.005	0.002	0.001	0.001	0.005	3,5
g_{tot} (m s ^{−1})	0.002	0.004	0.006	0.002	0.001	0.012	0.0018	0.001	0.001	0.003	3
g_{ch} (m s ^{−1})	0.08	0.08	0.01	0.01	0.04	0.04	0.04	0.04	0.04	0.04	6
b_1 (s m ^{−1})	208.3	133.3	57.7	85.8	202.0	178.6	0.2 ^a	790.9	175	105	3
b_2 (s m ^{−1})	8333.3	888.9	769.2	694.7	4040.4	178.6	24000 ^a	8181.8	2000	300	3
b_3	10	6	4.5	4	6.5	8	6.5 ^a	10	6	3	3

^aThe listed b_1 , b_2 , and b_3 values for the WSV biome are for the first segment of the fitted g_0 versus NDVI function when $\text{NDVI} \leq 0.64$. When $\text{NDVI} > 0.64$, the b_1 , b_2 , b_3 , and b_4 parameters are set to 57.1, 3333.3, 8, and -0.01035 , respectively; 1: Zhao *et al.* [2008]; 2: Mu *et al.* [2007]; 3: this study; 4: Larcher [2003]; 5: Monteith and Unsworth [2007]; 6: Thornton [1998].

conditions. These effects provide a negative feedback for transpiration so that stomatal conductance has less effect on canopy water loss at higher NDVI and canopy density levels than would be expected from an analysis of individual leaves [Jarvis and McNaughton, 1986]. The error bars show that there is variability in g_0 , which generally falls between 0.0005 and 0.002 m s^{-1} . The SV, WSV, and CSH biomes have the lowest variability in g_0 ; EBF, DBF, and CRP biomes have the highest g_0 variability, and TENF, BENF, OSH and GRS biomes show intermediate g_0 variability. The fitted g_0 versus NDVI functions using the means of g_0 should not significantly affect ET estimates considering the generally low variability in g_0 .

[32] The derived g_0 versus NDVI relationships for the 10 biome types show clear differences among each other despite having similar functional shapes; these differences reflect variations in leaf traits and physiologies among the different biome types. The relationship between g_0 and NDVI for the TENF group shows an upward shift relative to the BENF group, indicating that climate influences leaf traits and physiological responses within the broader ENF biome type. The g_0 values generally vary between 0.001 and 0.012 m s^{-1} and are biome specific. For the same values of NDVI, g_0 values are highest for the EBF and DBF biome types followed by the CRP, GRS, TENF, and BENF types, while the CSH, OSH, WSV, and SV types have the lowest g_0 values. These results are similar to reported values of maximum stomatal conductance determined for 15 global flux towers by Leuning *et al.* [2008]. We applied sigmoid functions to describe the observed relationship between g_0 and NDVI in Figure 2. The fitted curves for the 10 biome types are also shown in Figure 2 and show generally favorable agreement with the tower observations. The fitted curves explain 81%, 55%, 77%, 55%, 54%, 24%, 86%, 31%, 77%, and 60% of the variation in g_0 for the BENF, TENF, EBF, DBF, CSH, OSH, WSV, SV, GRS, and CRP types, respectively. The derived 99% posterior distributions of the g_0 versus NDVI relationships are generally narrow for each biome type (Figure 2). However, there are large uncertainties in these relationships at higher NDVI values (>0.80) for several biome types, including EBF, DBF, CSH, WSV, and GRS; this is due to less data and larger variations in the relationships between g_0 and NDVI at these higher canopy densities. The larger uncertainties in the fitted g_0 versus NDVI relationships at these higher NDVI levels may introduce larger uncertainties in the corresponding LE/ET calculations.

4.2. ET Algorithm Performance Relative to Tower Measurements

4.2.1. Development Tower Set Results

[33] We produced two sets of daily LE estimates at the tower level. The first set was produced using tower-measured meteorology (hereafter called tower-driven results), while the second set was produced using daily NNR meteorology and NASA/GWEX SRB solar radiation inputs (hereinafter called reanalysis-driven results). We then compared these algorithm results with corresponding ET measurements from the respective flux towers. The statistical summaries of ET algorithm performance for the development sites are plotted in Figure 3. The MR statistics of the tower-driven daily LE estimates are within $\pm 20 \text{ W m}^{-2}$, while

RMSE values are below 32 W m^{-2} for all 34 sites (Figure 3). The correlation coefficients between tower-driven daily LE estimates and daily LE observations are higher than 0.6. The lowest r value is 0.649 at the USWRC site (Figure 3). Overall, there is no substantial difference in ET algorithm performance among the different biome types.

[34] The daily LE simulations driven by NNR meteorology and NASA/GEWEX SRB solar radiation inputs are similar to the results derived from the tower-measured meteorology. However, the reanalysis-driven simulations have generally larger MR and RMSE differences and lower correlation coefficients relative to the tower-derived results, which are attributed to differences between the coarse ($1.9^\circ \times 1.875^\circ$ resolution) NNR meteorology and NASA/GEWEX SRB solar radiation (at the $1.0^\circ \times 1.0^\circ$ resolution) and local micrometeorology within the tower footprints. Insufficient representation of local tower meteorological conditions by the coarser NNR and/or NASA/GEWEX SRB inputs substantially reduce accuracy of the reanalysis-driven daily LE estimates at several sites, including USBLO, AUWAC, BRSA1, USSRM, and USAUD. However, this does not necessarily mean that the reanalysis-driven LE estimates have large biases and uncertainties at regional scales because these results may actually be more representative of surrounding landscape conditions than the local tower footprint.

[35] The daily time series of modeled LE fluxes derived from tower-measured meteorology and meteorology reanalysis inputs are plotted with corresponding tower LE measurements in Figure 4 for representative tower sites from the algorithm development set. Each of the selected towers represents the longest measurement record for the respective biome type. There are some uncertainties in the model results at several sites. For example, both sets of model results at CAOBS tend to underestimate mid-season ET values. There are many low LE values in summer from the reanalysis-driven ET results at USBLO, which are caused by considerable overestimation of NNR VPD inputs for this period. Overall, both sets of model results generally agree well with tower observations and capture observed LE seasonality and interannual variability and associated differences among the global biomes represented.

4.2.2. Validation Tower Set Results

[36] ET algorithm performance for the validation tower set was similar to the results from the algorithm development tower set (Figure 5), although the MR and RMSE statistics for the validation set have slightly wider distributions than the algorithm development set. The MR values of the tower-driven daily LE estimates fall within $\pm 20 \text{ W m}^{-2}$ for 44 sites and within $\pm 30 \text{ W m}^{-2}$ for the remaining four validation sites (Figure 5). The RMSE values of tower-driven LE estimates are below 45 W m^{-2} for all 48 validation sites, of which 45 sites have RMSE differences below 32 W m^{-2} (Figure 5). Correlation coefficients between tower meteorology based daily LE estimates and tower observations are generally higher than 0.6, while the lowest r value is 0.24 for the USSO2 site (Figure 5).

[37] The reanalysis-driven daily LE simulations have similar accuracies as the tower-driven results for most sites but markedly lower accuracies at some sites due to differences between reanalysis and local tower meteorology. Figure 6 shows the time series of modeled daily LE fluxes driven by tower measurements and reanalysis inputs with

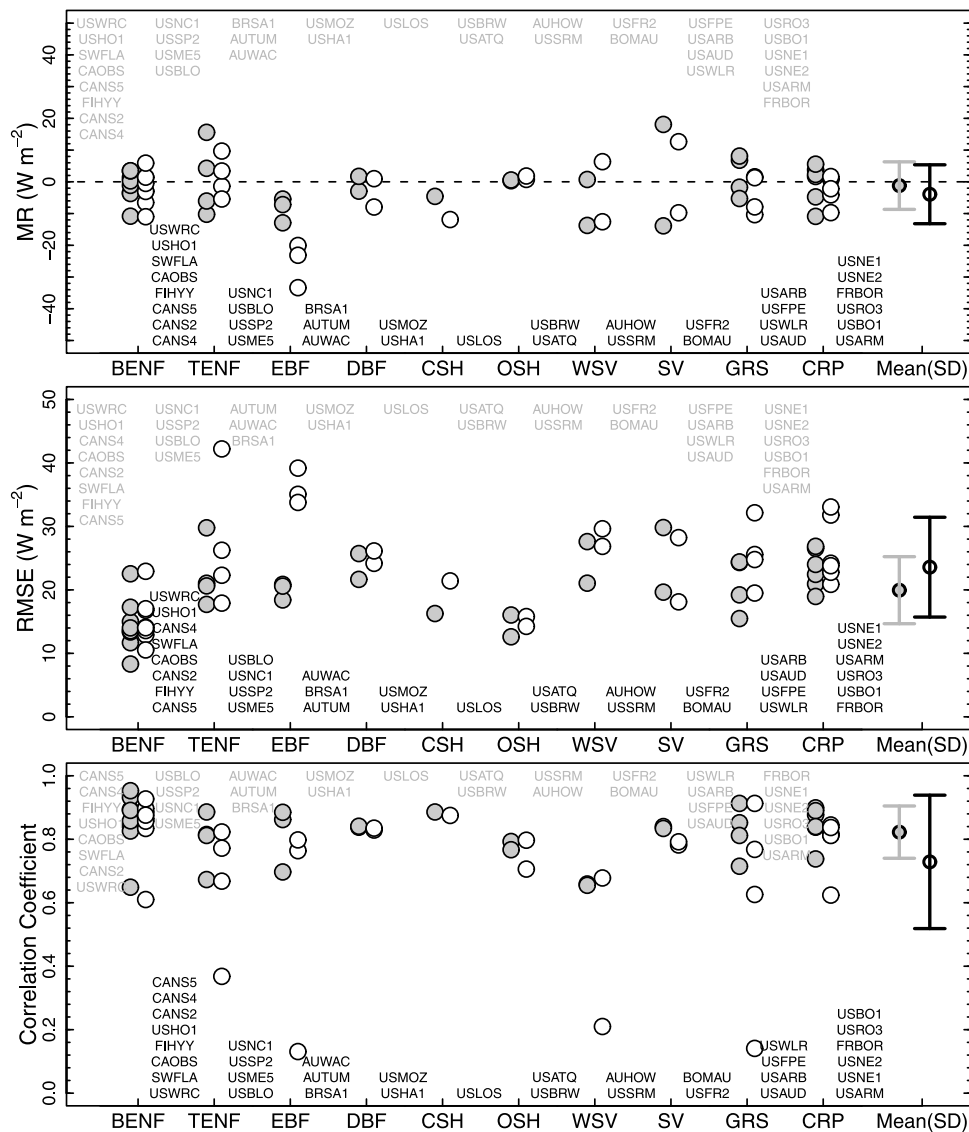


Figure 3. Comparisons of modeled and measured daily LE for the 34 algorithm development tower sites. The statistics include mean residual (Observation-Estimate) (MR), root mean square error (RMSE), and correlation coefficient (r) between modeled and measured values. The modeled results include estimates driven by (1) tower-measured meteorology (closed circles in gray) and (2) NNR meteorology (open circles). The site names are labeled in gray from top to bottom in the same order of the corresponding statistical values for the tower-driven results in each panel, while the site names are listed in black from bottom to top for the reanalysis-driven results in each frame. The cross-site means and standard deviations of the three statistics are also plotted. All r values are significant with 99% confidence.

corresponding tower LE measurements for representative tower sites from the validation set. Each of the selected towers represents one biome type with the longest record within the respective tower group. There are large differences between modeled and measured LE values at several sites. For the USNR1 site, there are many measured high LE values during winters in 1999, 2000, 2001, and 2002, but these patterns do not show in the following years, indicating that the large winter LE variations in the earlier years may be an artifact of measurement errors. Both tower-driven and reanalysis-driven results tend to overestimate LE during the early seasons at USKS2 but underestimate LE during the middle seasons at CAOAS. The low correlations between LE simulations and LE measurements at USSO2 are to some

extent due to lack of variation in satellite-observed NDVI and small LE sample size for comparison. Moreover, this site is located in the California Mediterranean climate zone where plant transpiration can be greatly impacted by occasional precipitation and fog events that are not directly captured in our ET algorithms. Despite these uncertainties in the LE simulations, both sets of model results generally correspond well with the tower observations and capture observed LE seasonality and interannual variability and associated differences among the major global biomes represented.

[38] For MF tower sites, LE/ET was computed as a weighted composite of all forest types within the tower footprint including ENF, EBF, DNF, and DBF, as deter-

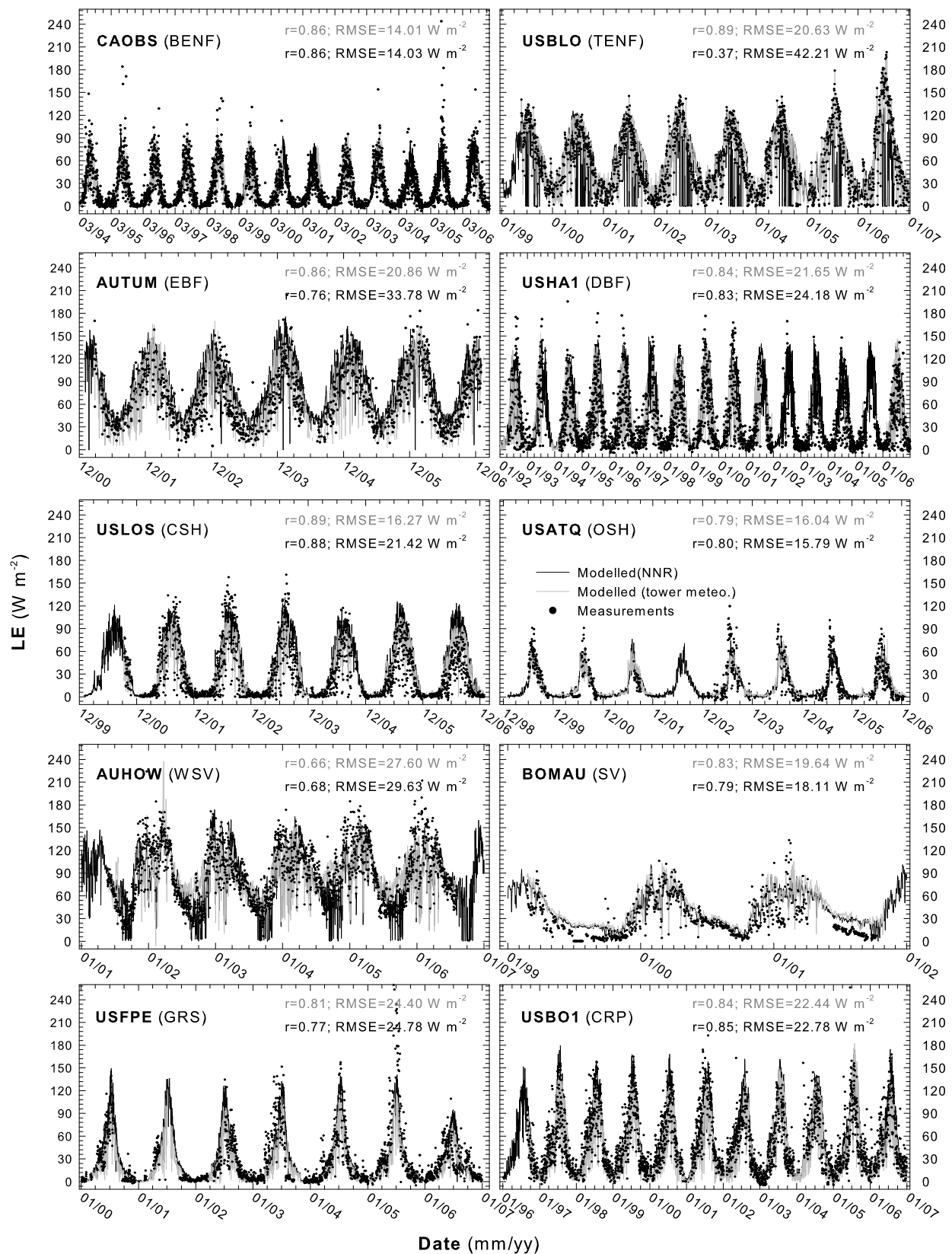


Figure 4. Time series of daily measured and modeled latent heat flux (LE: W m^{-2}) using the NDVI-based ET algorithm driven by tower-measured and NNR meteorology for the representative tower sites with the longest (3–15 years) records for their respective land cover classes from the algorithm development tower set. The r and RMSE statistics are also listed for the two sets of simulations for each site. All r values are significant with 99% confidence. The time series and statistics of modeled LE driven by tower-measured and NNR meteorology are marked in gray and black, respectively.

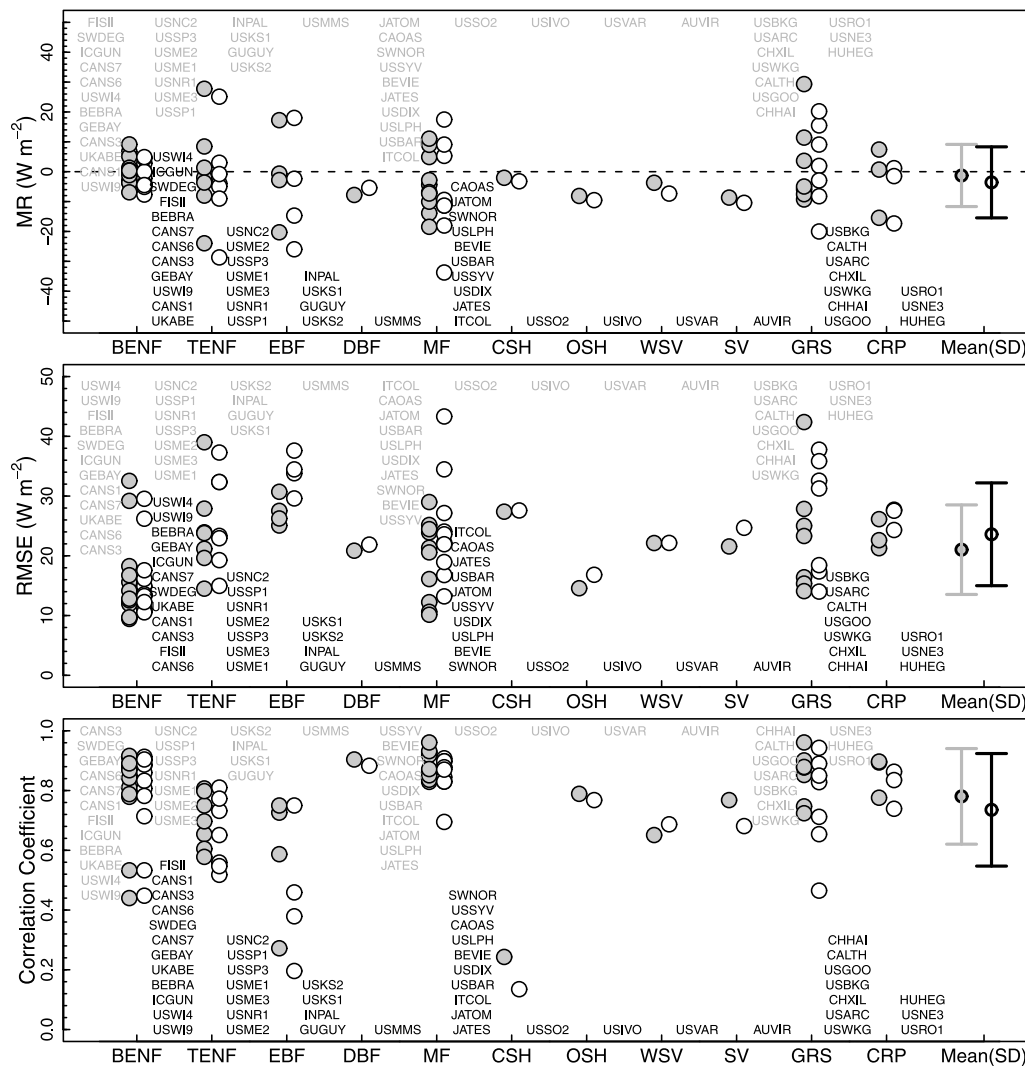


Figure 5. Comparisons of modeled and measured daily latent heat flux at the 48 validation tower sites. The meanings of the symbols and the organization of the graphs are the same as those in Figure 3. All r values are significant with 99% confidence.

mined from satellite remote sensing–based tree cover continuous fields data. This method accounts for the effects of varying tree compositions on the aggregate functional response of mixed forest stands and was evaluated at 10 MF tower sites across the global domain, including 3, 2, and 5 sites in Europe, Asia, and North America, respectively (Table 2). The two sets of simulations driven by tower and reanalysis meteorology inputs at these MF tower sites show generally similar LE/ET accuracies as non MF tower sites, with higher correlation coefficients than some biome types (Figure 5).

4.2.3. Evaluation of Monthly ET Estimates

[39] On a monthly basis, the model ET results derived from both tower-measured and reanalysis meteorology inputs agree well with ET observations from the 82 tower sites, including both algorithm development and validation sets (Figure 7). The tower-driven results account for approximately 84% of the observed variation in monthly ET measurements with respective RMSE and MR differences of 13.0 and $-0.8 \text{ mm month}^{-1}$, while the reanalysis-derived results

account for 80% of the variation in measured ET with respective RMSE and MR values of 15.3 and $-3.0 \text{ mm month}^{-1}$. The local tower conditions were poorly represented by the coarse NNR meteorology at several sites, reducing the overall performance of reanalysis-driven results. The USSRM site located in Arizona's arid area is the most obvious example. The coarse NNR meteorology poorly captures the air vapor pressure around this woody savanna site, resulting in substantial underestimates of ET and the flat distribution of the scatter points (solid triangles) in the lower left portion of Figure 7b. However, the reanalysis-driven results show similar performance relative to tower-driven results at most sites. Although the model results show small global biases for both algorithm development and validation sets, the high coefficients of determination (i.e., R^2), low RMSE, and MR differences for the two sets of monthly ET results indicate that the algorithm generally captures observed seasonal and inter-annual variations and site-to-site differences in ET.

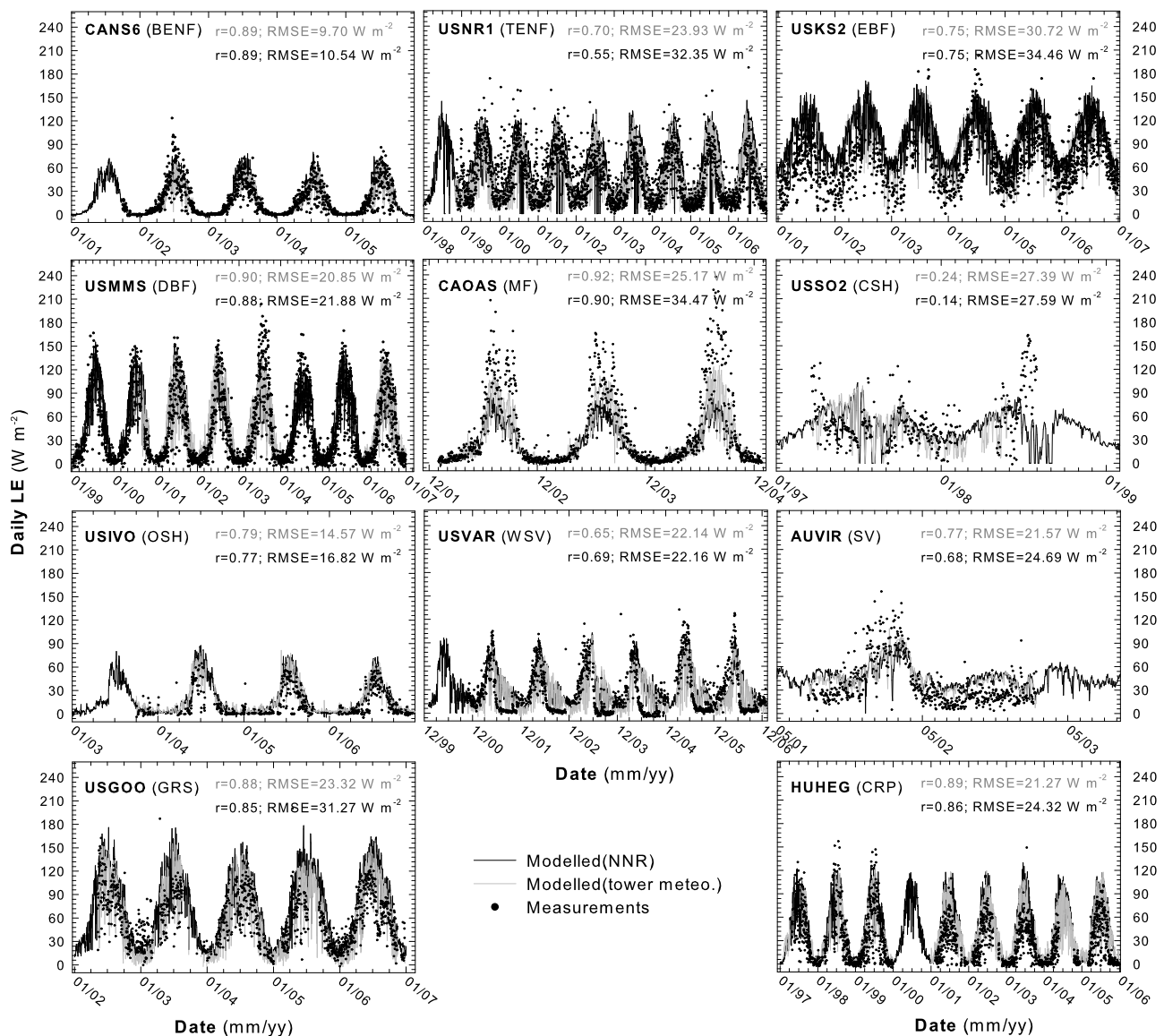


Figure 6. Time series of daily measured and modeled latent heat flux (LE: W m^{-2}) using the NDVI-based ET algorithm driven by tower-measured and NNR meteorology for representative tower sites with the longest (2–9 years) measurement records in their respective land cover classes from the validation tower set. The r and RMSE statistics are also listed for the two sets of simulations for each site. All r values are significant with 99% confidence. The time series and statistics of modeled LE driven by tower-measured and NNR meteorology are marked in grey and black, respectively.

4.3. Evaluation of ET at the Basin Level

[40] The satellite-based global ET results were evaluated against inferred basin-scale average ET derived from observed discharge and gauge-based (GPCC) precipitation records for 261 global basins (Figure 8). Figure 8a shows the global distribution of selected basins and the relative difference (%) between ET_{RS} and $\text{ET}_{\text{Inferred}}$ defined as $(\text{ET}_{\text{RS}} - \text{ET}_{\text{Inferred}}) \times 100 / \text{ET}_{\text{Inferred}}$. Figure 8b is the scatter plot of the relationship between ET_{RS} and $\text{ET}_{\text{Inferred}}$; these results indicate that ET_{RS} and $\text{ET}_{\text{Inferred}}$ are similar for most basins (RMSE = 186.3 mm yr^{-1} ; $R^2 = 0.80$). The relative difference between ET_{RS} and $\text{ET}_{\text{Inferred}}$ falls within $\pm 50\%$, $\pm 20\%$, and $\pm 10\%$ for 95%, 68%, and 47% of the area covered by the 261 basins, respectively. The largest ET_{RS} and $\text{ET}_{\text{Inferred}}$ difference occur in some northern high lati-

tude, subtropical and tropical basins (Figure 8a). ET_{RS} is much higher than $\text{ET}_{\text{Inferred}}$ in some northern high-latitude basins including the Yukon, Mackenzie, Yenisei, Lena, Kolyma, Pechora, Indigirka, and Yana basins (Figure 8a). The mean ET_{RS} and $\text{ET}_{\text{Inferred}}$ difference in these basins is approximately 100 mm yr^{-1} . This systematic difference is at least partially attributable to the substantial underestimation of GPCC precipitation from snow and wind-related biases of gauge observations and the sparse weather station network density in the northern high latitudes [Yang *et al.*, 2005]. Zhang *et al.* [2009] showed that the GPCC product underestimates precipitation by $7.15 \text{ mm month}^{-1}$ in relation to bias-corrected observations in these regions [Yang *et al.*, 2005]. The GPCC precipitation bias can contribute to an underestimation of 90 mm yr^{-1} in $\text{ET}_{\text{Inferred}}$, which

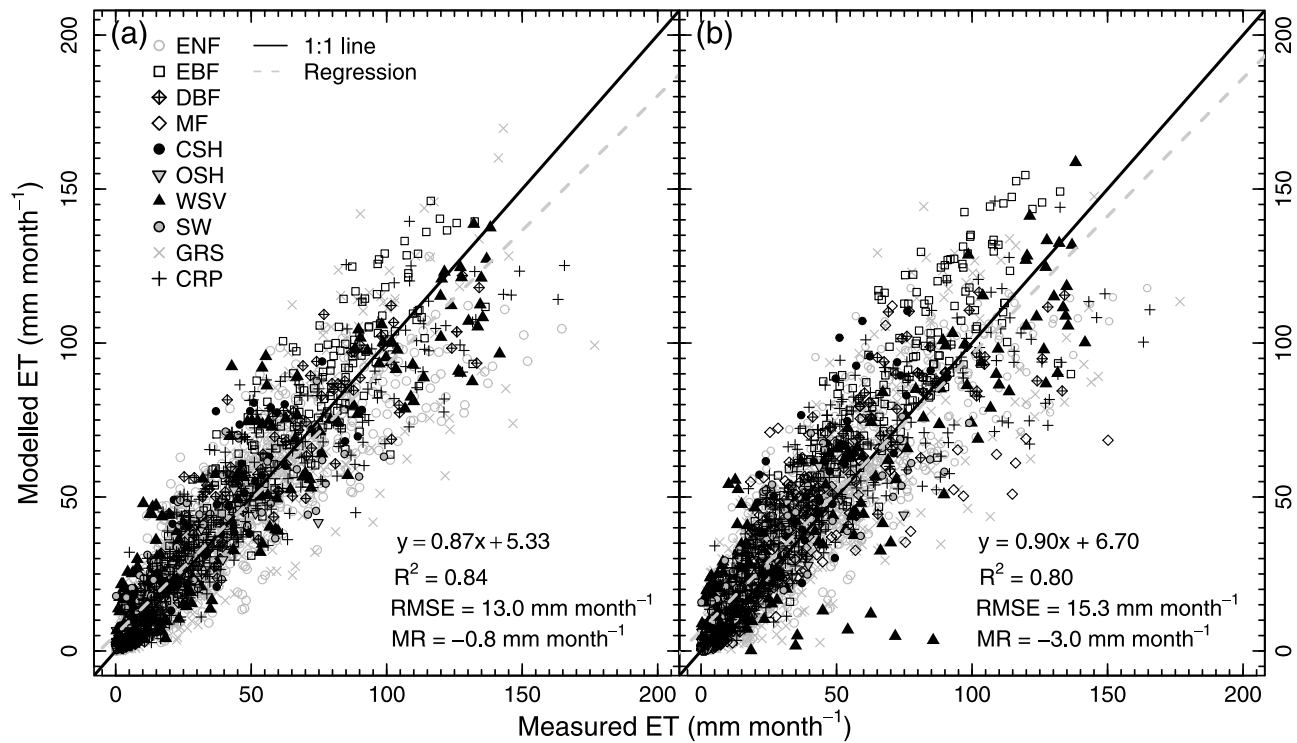


Figure 7. Comparisons between monthly modeled ET (mm month^{-1}) and tower measurements for the 82 tower sites; the simulations in Figure 7a are derived from tower-measured meteorology, while simulations in Figure 7b are derived from NNR meteorology and NASA/GEWEX SRB solar radiation inputs. These relationships are significant with 99% confidence.

approximates the average difference between ET_{RS} and $ET_{Inferred}$ in these basins. ET_{RS} is lower than $ET_{Inferred}$ in Western Africa and Indian subcontinent basins, indicating that the RS model may underestimate actual ET in these regions. However, uncertainty in the coarse GPCC precipitation and discharge measurements may also contribute to ET_{RS} and $ET_{Inferred}$ differences in these regions. Although there are large differences between ET_{RS} and $ET_{Inferred}$ in

some basins, the generally favorable agreement in these results for most areas indicates that the RS-based ET product is relatively accurate on a global basis.

4.4. Reanalysis Meteorology Impacts on LE Estimation

[41] Overall, the NNR temperature variables (T_{max} , T_{avg} , and T_{min}) show the highest correspondences with the tower

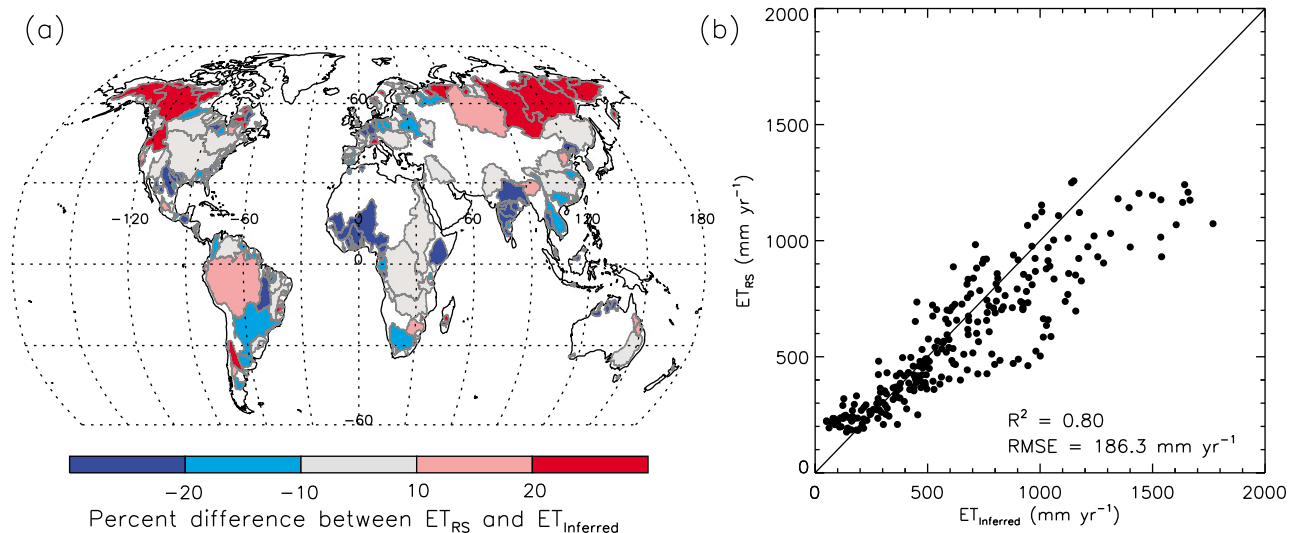


Figure 8. Comparisons between multiyear (1983–2006) average RS-based ET (ET_{RS}) and inferred ET ($ET_{Inferred}$) from basin-scale water balance calculations for 261 major global basins: (a) difference (%) between ET_{RS} and $ET_{Inferred}$ and (b) scatter plot of ET_{RS} versus $ET_{Inferred}$.

Table 4. Statistics for the Comparison of Daily NNR Meteorological Variables and NASA/GEWEX SRB Net Radiation Relative to Daily Tower Observations^a

Variables	MR	Q_1	M	Q_3	RMSE	R^2
T_{\max} (°C)	-0.08	-2.44	0.08	2.48	4.32	0.90
T_{avg} (°C)	0.10	-1.65	0.05	1.81	3.17	0.94
T_{\min} (°C)	-0.11	-2.39	-0.29	2.06	4.08	0.90
VPD (Pa)	-84.49	-225.94	-9.49	120.17	464.81	0.68
R_n (W m ⁻²)	-1.71	-20.47	-3.94	13.97	34.01	0.77

^aThe sample size for each variable is 97,655. The statistics include mean (MR), median (M), first quartile (Q_1), and third quartile (Q_3) of the errors defined as the measured values minus the reanalysis values, root mean squared error (RMSE), and coefficient of determination (R^2).

observations and explain 90% or more of variability in the observations, while the NNR VPD explains the lowest variability in the tower site observations (Table 4); the correspondence (R^2) between tower observations and NASA/GEWEX SRB results for R_n is generally intermediate between these results. The error distributions for the temperature variables are also narrow, and the mean errors for these temperature variables are close to zero. Both NNR VPD and NASA/GEWEX SRB-based R_n are generally overestimated relative to the observations and show considerable error distributions. The statistics in Table 4 suggest that the largest uncertainties in input meteorological parameters are from NNR VPD followed by SRB based R_n , while the NNR temperature variables have the lowest uncertainties. These results are also consistent with previous studies [Zhang *et al.*, 2007; K. Zhang *et al.*, 2008].

[42] The effects of uncertainties in the five meteorological variables on LE/ET calculations are site specific. The correlations of RMSD(LE) with RMSD(T_{\max}), RMSD(T_{avg}), RMSD(T_{\min}), RMSD(VPD), and RMSD(R_n) for the 82 flux tower sites are 0.21 ($P = 0.06$), 0.12 ($P = 0.29$), 0.02 ($P = 0.86$), 0.41 ($P < 0.001$), and 0.34 ($P = 0.002$), respectively, indicating that uncertainties in the meteorological inputs have variable impacts to reanalysis-derived LE accuracy at the different tower sites. For some sites, uncertainty in reanalysis-derived LE is mainly caused by uncertainty in a single meteorological variable, e.g., AUHOW, USNR1, and CAOAS sites. For other sites, uncertainty in reanalysis-derived LE is due to uncertainties in two or more meteorological variables, e.g., AUWAC, AUTUM, ITCOL, and CALTH sites. Overall, RMSD(LE) has the strongest correlation with RMSD(VPD), followed by RMSD(R_n) and RMSD(T_{\max}). However, RMSD(LE) does not show clear correspondence with RMSD(T_{avg}) or RMSD(T_{\min}). This is consistent with the above findings that the uncertainties in VPD and R_n are the major sources of uncertainty in the reanalysis-driven LE/ET estimates. Among the three variables, only RMSD(T_{\max}) showed a significant correlation ($r = 0.57$; $P < 0.001$) with DEM heterogeneity within the 100 km \times 100 km tower windows. Since temperature is highly sensitive to elevation and slope-aspect variations, greater topographic complexity surrounding individual towers reduces the correspondence between the coarse scale meteorological conditions represented by the NNR reanalysis and associated LE/ET simulations and local tower conditions. The NNR atmospheric humidity and NASA/GEWEX SRB products may be more impacted by accuracy in other forcing data including cloudiness, atmospheric aerosols, and atmospheric ozone concentrations [Kistler *et al.*, 2001; Pinker and Laszlo, 1992].

4.5. Global ET Patterns

[43] We applied the NDVI-based ET algorithm with daily NNR surface meteorology and NASA/GEWEX SRB solar radiation inputs to calculate daily ET globally at 8 km spatial resolution from 1983 to 2006. The multiyear (1983–2006) average annual ET is plotted in Figure 9 and shows strong regional variations and latitudinal gradients corresponding to global climate patterns. Tropical rainforests in South America, Africa, and Southeast Asia have the highest annual ET, while drier areas within temperate and subtropical regions and the Arctic have the lowest annual ET. Annual ET values for temperate and boreal forests are generally intermediate between these two extremes. The estimated ET over water bodies is generally much larger than for adjacent vegetated areas within the same climate zone due to lower surface resistance to evaporation over water relative to land. The global terrestrial average annual ET weighted by area is 539.3 ± 9.1 mm yr⁻¹, which is about 0.60 ± 0.02 of the global average annual GPCC precipitation. The estimated global average ET to P ratio is similar to values reported from previous studies [e.g., L'vovich and White, 1990; Alton *et al.*, 2009]. The Evergreen Broadleaf Forest biome has the largest average ET of 1138 ± 175 mm yr⁻¹ followed by Woody Savanna (749 ± 209 mm yr⁻¹), Deciduous Broadleaf Forest (635 ± 200 mm yr⁻¹), Savanna (676 ± 183 mm yr⁻¹), Permanent Wetland (529 ± 311 mm yr⁻¹), Cropland (507 ± 157 mm yr⁻¹), Mixed Forest (361 ± 124 mm yr⁻¹), Closed Shrubland (352 ± 166 mm yr⁻¹), Grassland (311 ± 193 mm yr⁻¹), Evergreen Needleleaf Forest (294 ± 81 mm yr⁻¹), Deciduous Needleleaf Forest (243 ± 29 mm yr⁻¹), and Open Shrubland (202 ± 83 mm yr⁻¹). Open water bodies cover about 3.4% of the global land area as inferred by the 500 m MODIS-IGBP land cover product, while mean annual ET from these water bodies is 906 ± 561 mm yr⁻¹ and represents approximately 7% of total annual terrestrial ET.

[44] The magnitudes and spatial patterns of the estimated global ET are generally consistent with the literature. The study of Bruijnzeel [1990] indicated that annual ET ranges from 1310 to 1500 mm in humid tropical forests. Frank and Inouye [1994] used 19–25 year climate records to calculate annual ET at 94 sites representing 11 biomes and reported annual ET of 202 ± 34 , 380 ± 43 , 588 ± 47 , 884 ± 71 , and 1363 ± 77 mm yr⁻¹ for tundra (10 sites), taiga (11 sites), broadleaf forest (10 sites), savannah (4 sites), and wet tropical forest (10 sites), respectively. Measurements of water vapor fluxes from 1 September 2003 to 31 August 2004 in a 74 year mixed-wood boreal forest in Ontario, Canada, show an annual water loss of 480 ± 30 mm [Pejam *et al.*, 2006]. Giambelluca *et al.* [2009] reported mean annual ET values of 823 and 689 mm for two tropical savanna sites in central Brazil using tower eddy covariance measurements. Eddy covariance measurements for a poplar plantation in Northern Italy revealed cumulative ET over three growing seasons (April–September) of 388, 471, and 484 mm for 2002, 2003, and 2004, respectively [Migliavacca *et al.*, 2009].

[45] The multiyear mean seasonal patterns of ET from 1983 to 2006 using the NDVI-based ET algorithm with daily NNR surface meteorology and NASA/GEWEX SRB solar radiation inputs shows distinct global seasonality (Figure 10). The tropical rain forest regions show year-round high ET values, while tropical dry forest and savanna regions show alternate wet and dry seasons. The temperate

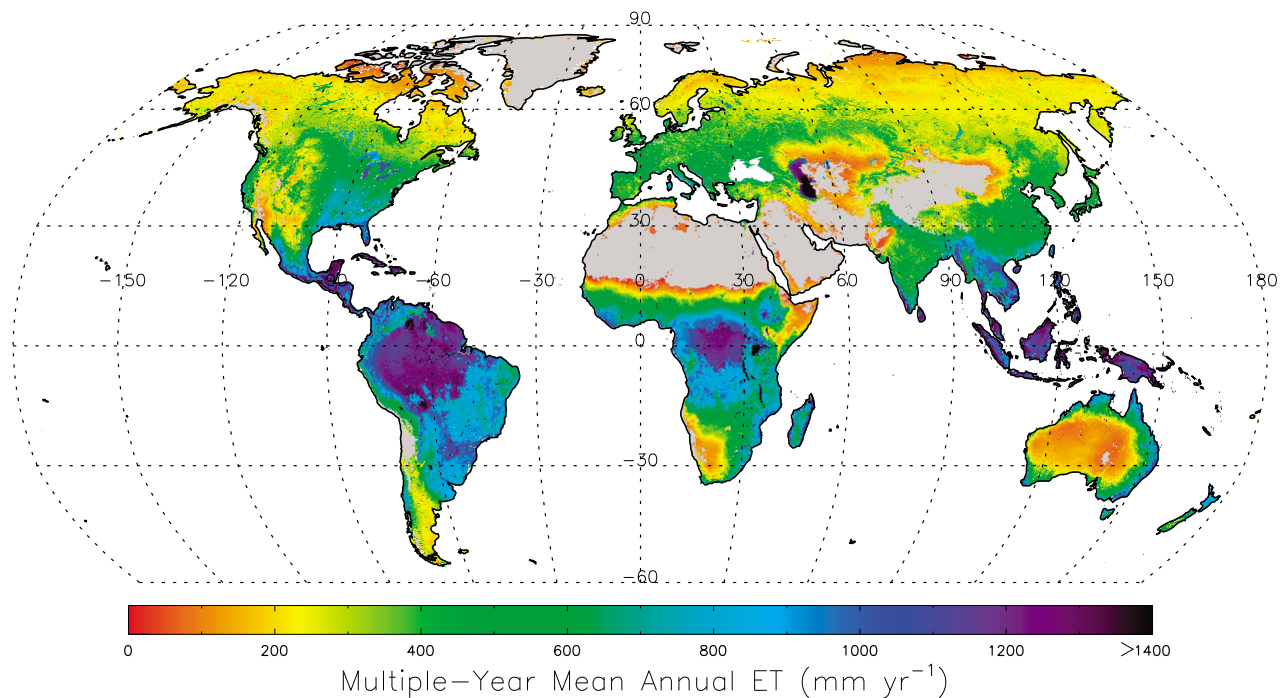


Figure 9. Global map of multiyear (1983–2006) mean annual ET as derived from the AVHRR GIMMS NDVI record, NNR daily meteorology, and NASA SRB solar radiation inputs. Barren land (in gray) and ocean (in white) areas were excluded from the model calculations.

and boreal-Arctic regions have much higher seasonal variability than the tropics.

5. Discussion and Conclusions

[46] We extended an NDVI-based ET algorithm, originally developed for the northern high latitudes [Zhang *et al.*,

2009], to the global domain by deriving biome-specific maximum canopy conductance functions for all major global biomes. The algorithm was modified using AVHRR GIMMS NDVI and corresponding tower eddy-covariance measurement derived canopy conductances from 34 globally distributed sites. The algorithm was applied using two sets of

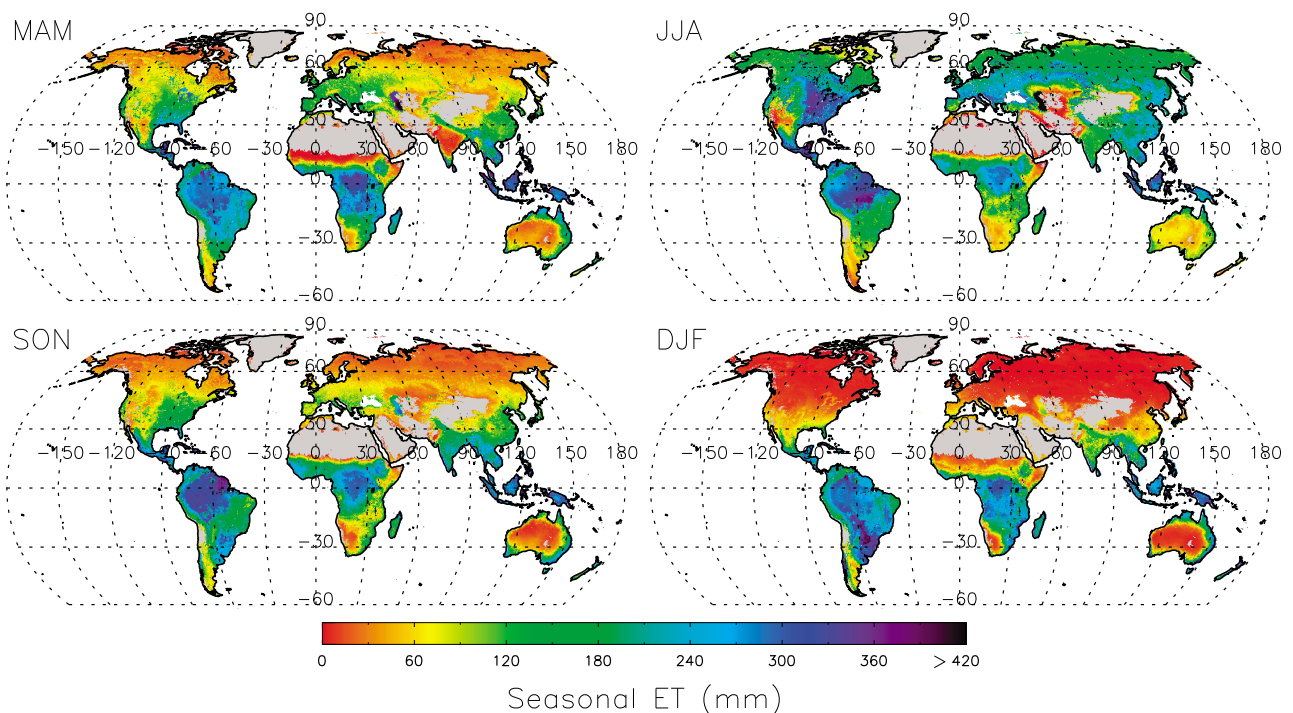


Figure 10. Multiyear (1983–2006) mean seasonality of global ET.

daily meteorology inputs, including in situ tower measurements and relatively coarse-resolution NNR and NASA/GEWEX SRB gridded global products. The model was validated using tower ET measurements at the 34 development sites and 48 additional, independent tower sites encompassing the major global biomes. The AVHRR NDVI versus corresponding tower measurement derived potential canopy conductance values follow sigmoid-type response curves for the major biome types but with distinct differences among different biomes that follow characteristic variations in climate and associated plant adaptations; these results indicate that the NDVI-based canopy conductance algorithm is robust and more biophysically based than alternative approaches that employ a constant, maximum canopy conductance parameterization for individual biomes. The two sets of LE/ET simulations at the tower level show generally favorable agreement with tower measurements at daily and monthly time scales, although the tower-driven results show generally better accuracy than the reanalysis-driven results. These results indicate that the ET algorithm provides a reasonably accurate measure of spatial patterns and daily to annual temporal dynamics in global ET and corresponding land-atmosphere water and latent energy exchanges. The global ET results capture observed spatial and temporal variations at the global scale and compare favorably with ET inferred from basin-scale water balance calculations for 261 basins covering 61% of the global vegetated area. Through this study, we constructed an ET climatology based on long-term satellite observations for each pixel of the global vegetated land area.

[47] Two potential sources of uncertainty in the ET calculations are linked to corresponding uncertainties in tower eddy flux measurements and satellite-observed NDVI used for model development and validation. First, we used the 8 km AVHRR GIMMS NDVI record to derive NDVI values at each tower site. The tower measurement footprints are typically about 1 km in size [Baldocchi, 2008] and much smaller than the resolution of the overlying GIMMS NDVI grid cell. The satellite derived NDVI may not adequately capture subgrid scale vegetation signals at these sites, especially in areas of complex topography or heterogeneous land cover; thus, model error for some tower sites may be attributed to inaccurate NDVI representation of tower footprint conditions. The ET algorithm performance may also be negatively impacted by uncertainty in tower eddy flux measurements and associated lack of energy balance closure due to complexity in wind patterns, footprint representation and sampling variability [Twine *et al.*, 2000; Wilson *et al.*, 2002]. Twine *et al.* [2000] reported that the discrepancy in energy balance closure is generally about 10%–30% when the eddy covariance method is used. These tower measurement uncertainties are within the range of accuracy of the algorithm ET calculations but may also introduce additional model error because tower LE measurements are used to derive biome-specific relationships between g_0 and NDVI. In addition, the ET algorithm in this study does not explicitly consider the impacts of precipitation events on surface conductances due to the limited availability of accurate global precipitation data, which may introduce ET estimation uncertainty.

[48] Despite the above uncertainties, the ET algorithm performs well across the observed range of global biomes, vegetation conditions, and climatic regimes as indicated by

favorable agreement with LE/ET measurements from 82 diverse tower sites, annual ET values reported in the literature and basin scale ET estimates inferred from the regional water balance. The algorithm is also simple enough to apply with long-term global satellite NDVI records for evaluating regional ET anomalies and climatologies, drought, agricultural, and forest health monitoring and other applications. The results of this study also represent a systematic and continuous long-term (24 year) global record of ET/LE with well-quantified accuracy useful for global assessment of ET climatologies and climate change assessment of terrestrial water and energy cycle dynamics and interactions.

[49] **Acknowledgments.** This work was supported by the NASA Hydrology, Terrestrial Ecology, and Earth System Science Fellowship programs. The flux tower measurement data were provided by AmeriFlux, ORNL-DAAC, and individual tower site principal investigators. We gratefully acknowledge all tower site principle investigators and their teams for providing the evaporation and meteorological data used in this study. The NASA/GEWEX solar radiation data were obtained from the NASA Langley Research Center Atmospheric Science Data Center. We also gratefully acknowledge MATLAB code developed by Hieki Haario and associates, Lappeenranta U. of Technology, Helsinki, Finland, and their work in adaptive MCMC methods.

References

- Allen, R. G., L. S. Pereira, D. Raes, and M. Smith (1998), *Crop Evapotranspiration: Guidelines for Computing Crop Requirements*, FAO Irrigation and Drainage Paper 56, Food and Agricultural Organization of the U.N., Rome.
- Alton, P., R. Fisher, S. Los, and M. William (2009), Simulation of global evapotranspiration using semiempirical and mechanistic schemes of plant hydrology, *Global Biogeochem. Cycles*, 23, GB4023, doi:10.1029/2009GB003540.
- Anderson, M. C., J. M. Norman, W. P. Kustas, R. Houborg, P. J. Starks, and N. Agam (2008), A thermal-based remote sensing technique for routine mapping of land-surface carbon, water and energy fluxes from field to regional scales, *Remote Sens. Environ.*, 112, 4227–4241.
- Aubinet, M., B. Chermanne, M. Vandenhaute, B. Longdoz, M. Yernaux, and E. Laitat (2001), Long term carbon dioxide exchange above a mixed forest in the Belgian Ardennes, *Agr. Forest Meteorol.*, 108, 293–315.
- Baker, J. M., T. E. Ochsner, R. T. Venterea, and T. J. Griffis (2007), Tillage and soil carbon sequestration – What do we really know? *Agr. Ecosyst. Environ.*, 118, 1–5.
- Baldocchi, D. (2008), Breathing of the terrestrial biosphere: Lessons learned from a global network of carbon dioxide flux measurement systems, *Aust. J. Bot.*, 56, 1–26.
- Barcza, Z., A. Kern, L. Haszpra, and N. Kljun (2009), Spatial representativeness of tall tower eddy covariance measurements using remote sensing and footprint analysis, *Agr. Forest Meteorol.*, 149, 795–807.
- Barr, A. G., K. Morgenstern, T. A. Black, J. H. McCaughey, and Z. Nesic (2006), Surface energy balance closure by the eddy-covariance method above three boreal forest stands and implications for the measurement of the CO₂ flux, *Agr. Forest Meteorol.*, 140, 322–337.
- Bastiaanssen, W. G. M., M. Menenti, R. A. Feddes, and A. A. M. Holtslag (1998), A remote sensing surface energy balance algorithm for land (SEBAL): 1. Formulation, *J. Hydrol.*, 212–213, 198–212.
- Berbigier, P., and D. Lousteau (2000), Bordeaux, France, The Euroflux dataset 2000, in *Carbon, Water and Energy Exchanges of European Forests*, edited by R. Valentini, p. 300, Springer-Verlag, Heidelberg.
- Beringer, J., L. B. Hutley, N. J. Tapper, and L. A. Cernusak (2007), Savanna fires and their impact on net ecosystem productivity in North Australia, *Global Change Biol.*, 13, 990–1004.
- Bonal, D., et al. (2008), Impact of severe dry season on net ecosystem exchange in the Neotropical rainforest of French Guiana, *Global Change Biol.*, 14, 1917–1933.
- Bouchet, R. J. (1963), Evapotranspiration réelle evapotranspiration potentielle, signification climatique, *Proc. Berkeley Calif. Symp. IAHS Publ.*, 62, 134–142.
- Bruijnzeel, L. A. (1990), *Hydrology of Moist Tropical Forests and Effects of Conversion: A State of Knowledge Review*, International Hydrological Programme, UNESCO, Paris, France.

- Ceulemans, R. (2000), Braschaat, Belgium, The Euroflux dataset 2000, in *Carbon, Water and Energy Exchanges of European Forests*, edited by R. Valentini, p. 300, Springer-Verlag, Heidelberg.
- Choudhury, B. J., and N. E. DiGirolamo (1998), A biophysical process-based estimate of global land surface evaporation using satellite and ancillary data: I. Model description and comparison with observations, *J. Hydrol.*, **205**, 164–185.
- Clark, K. L., N. Skowronski, and J. Hom (2010), Invasive insects impact forest carbon dynamics, *Global Change Biol.*, **16**, 88–101.
- Clement, R., J. B. Moncrieff, and P. G. Jarvis (2003), Net carbon productivity of Sitka Spruce forest in Scotland, *Scottish Forestry*, **57**, 5–10.
- Cleugh, H. A., R. Leuning, Q. Mu, and S. W. Running (2007), Regional evaporation estimates from flux tower and MODIS satellite data, *Remote Sens. Environ.*, **106**, 285–304.
- Cook, B. D., et al. (2004), Carbon exchange and venting anomalies in an upland deciduous forest in northern Wisconsin, USA, *Agr. Forest Meteorol.*, **126**, 271–295.
- Coulter, R. L., M. S. Pekour, D. R. Cook, G. E. Klazura, T. J. Martin, and J. D. Lucas (2006), Surface energy and carbon dioxide fluxes above different vegetation types within ABLE, *Agr. Forest Meteorol.*, **136**, 147–158.
- Dai, A., T. T. Qian, K. E. Trenberth, and J. D. Milliman (2009), Changes in continental freshwater discharge from 1948 to 2004, *J. Climate*, **22**, 2773–2792.
- DeForest, J. L., G. Sun, A. Noormets, J. Chen, S. McNulty, M. Gavazzi, D. M. Amatya, and R. W. Skaggs (2006), Carbon and water fluxes in a drained coastal clearcut and a pine plantation in eastern North Carolina, in *Hydrology and Management of Forested Wetlands: Proceedings of the International Conference*, edited by T. M. William and J. Nettles, pp. 587–597, *Am. Soc. Agr. Biol. Eng.*, St. Joseph, MI.
- DeFries, R. S., M. Hansen, J. R. G. Townshend, A. C. Janetos, and T. R. Loveland (2000a), 1 kilometer tree cover continuous fields, 1.0, Department of Geography, University of Maryland, College Park, Maryland, 1992–1993.
- DeFries, R. S., M. C. Hansen, J. R. G. Townshend, A. C. Janetos, and T. R. Loveland (2000b), A new global 1 km dataset of percentage tree cover derived from remote sensing, *Global Change Biol.*, **6**, 247–254.
- Dijkstra, P., et al. (2002), Elevated atmospheric CO₂ stimulates above-ground biomass in a fire-regenerated scrub-oak ecosystem, *Global Change Biol.*, **8**(1), 90–103.
- Dunn, A. L., and S. C. Wofsy (2006), *Boreal Forest CO₂ Flux, Soil Temperature, and Meteorological Data*, Department of Earth & Planetary Sciences, Cambridge, MA.
- Epstein, H. E., M. P. Calef, M. D. Walker, F. S. Chapin, and A. M. Starfield (2004), Detecting changes in Arctic tundra plant communities in response to warming over decadal time scales, *Global Change Biol.*, **10**, 1325–1334.
- Falk, M., S. Wharton, M. Schroeder, S. Ustin, and K. T. Paw U (2008), Flux partitioning in an old-growth forest: Seasonal and interannual dynamics, *Tree Physiol.*, **28**, 509–520.
- Ferguson, C. R., J. Sheffield, E. F. Wood, and H. Gao (2010), Quantifying uncertainty in a remote sensing-based estimate of evapotranspiration over the continental United States, *Int. J. Remote Sens.*, **31**(14), 3821–3865.
- Fischer, M. L., D. P. Billesbach, J. A. Berry, W. J. Riley, and M. S. Torn (2007), Spatiotemporal variations in growing season exchanges of CO₂, H₂O, and sensible heat in agricultural fields of the Southern Great Plains, Lawrence Berkeley Lab., Berkeley, CA.
- Fisher, J. B., K. P. Tu, and D. D. Baldocchi (2008), Global estimates of the land-atmosphere water flux based on monthly AVHRR and ISLSCP-II data, validated at 16 FLUXNET sites, *Remote Sens. Environ.*, **112**, 901–919.
- Frank, D. A., and R. S. Inouye (1994), Temporal variation in actual evapotranspiration of terrestrial ecosystems – Patterns and ecological implications, *J. Biogeogr.*, **21**, 401–411.
- Friedl, M. A., et al. (2010), MODIS collection 5 global land cover: Algorithm refinements and characterization of new datasets, *Remote Sens. Environ.*, **114**, 168–182.
- Giambelluca, T. W., F. G. Scholz, S. J. Bucci, F. C. Meinzer, G. Goldstein, W. A. Hoffmann, A. C. Franco, and M. P. Buchert (2009), Evapotranspiration and energy balance of Brazilian savannas with contrasting tree density, *Agr. Forest Meteorol.*, **149**, 1365–1376.
- Gillies, R. R., T. N. Carlson, J. Cui, W. P. Kustas, and K. S. Humes (1997), A verification of the 'triangle' method for obtaining surface soil water content and energy fluxes from remote measurements of the normalized difference vegetation index (NDVI) and surface radiant temperature, *Int. J. Remote Sens.*, **18**, 3145–3166.
- Gilmanov, T. G., L. L. Tieszen, B. K. Wylie, L. B. Flanagan, A. B. Frank, M. R. Haferkamp, T. P. Meyers, and J. A. Morgan (2005), Integration of CO₂ flux and remotely-sensed data for primary production and ecosystem respiration analyses in the Northern Great Plains: Potential for quantitative spatial extrapolation, *Global Ecol. Biogeogr.*, **14**, 271–292.
- Glenn, E. P., A. R. Huete, P. L. Nagler, K. K. Hirschboeck, and P. Brown (2007), Integrating remote sensing and ground methods to estimate evapotranspiration, *Crit. Rev. Plant Sci.*, **26**, 139–168.
- Goldstein, A. H., et al. (2000), Effects of climate variability on the carbon dioxide, water, and sensible heat fluxes above a ponderosa pine plantation in the Sierra Nevada (CA), *Agr. Forest Meteorol.*, **101**, 113–129.
- Griffis, T. J., J. Zhang, J. M. Baker, N. Kljun, and K. Billmark (2007), Determining carbon isotope signatures from micrometeorological measurements: Implications for studying biosphere-atmosphere exchange process, *Bound.-Layer Meteorol.*, **123**, 295–316.
- Gu, L. H., et al. (2007), Influences of biomass heat and biochemical energy storages on the land surface fluxes and diurnal temperature range, *J. Geophys. Res.*, **112**, D02107, doi:10.1029/2006JD007425.
- Haario, H., M. Laine, A. Mira, and E. Saksman (2006), DRAM: Efficient adaptive MCMC, *Stat. Comput.*, **16**, 339–354.
- Hadley, J. L., P. S. Kuzeja, M. J. Daley, N. G. Phillips, T. Mulcahy, and S. Singh (2008), Water use and carbon exchange of red oak- and eastern hemlock-dominated forests in the northeastern USA: implications for ecosystem-level effects of hemlock woolly adelgid, *Tree Physiology*, **28**(4), 615–627.
- Heinsch, F. A., J. L. Heilman, K. J. McInnes, D. R. Cobos, D. A. Zuberer, and D. L. Roelke (2004), Carbon dioxide exchange in a high marsh on the Texas Gulf Coast: Effects of freshwater availability, *Agr. Forest Meteorol.*, **125**, 159–172.
- Hirano, T., H. Segah, T. Harada, S. Limin, T. June, R. Hirata, and M. Osaki (2007), Carbon dioxide balance of a tropical peat swamp forest in Kalimantan, Indonesia, *Global Change Biol.*, **13**, 412–425.
- Hobbins, M. T., J. A. Ramirez, and T. C. Brown (2001), The complementary relationship of regional evapotranspiration: An enhanced advection-aridity model, *Water Resour. Res.*, **37**(5), 1389–1403, doi:10.1029/2000WR900359.
- Hollinger, et al. (2004), Spatial and temporal variability in forest-atmosphere CO₂ exchange, *Global Change Biol.*, **10**, 1689–1706.
- Hong, Y., K. L. Hsu, S. Sorooshian, and X. G. Gao (2005), Improved representation of diurnal variability of rainfall retrieved from the Tropical Rainfall Measurement Mission Microwave Imager adjusted Precipitation Estimation From Remotely Sensed Information Using Artificial Neural Networks (PERSIANN) system, *J. Geophys. Res.*, **110**, D06102, doi:10.1029/2004JD005301.
- Hsu, K. L., X. G. Gao, S. Sorooshian, and H. V. Gupta (1997), Precipitation estimation from remotely sensed information using artificial neural networks, *J. Appl. Meteorol.*, **36**, 1176–1190.
- Huffman, G. J., et al. (2007), The TRMM multisatellite precipitation analysis (TMPA): Quasi-global, multiyear, combined-sensor precipitation estimates at fine scales, *J. Hydrometeorol.*, **8**, 38–55.
- Huntington, T. G. (2006), Evidence for intensification of the global water cycle: Review and synthesis, *J. Hydrol.*, **319**, 83–95.
- Hutya, L. R., et al. (2007), Seasonal controls on the exchange of carbon and water in an Amazonian rain forest, *J. Geophys. Res.*, **112**, G03008, doi:10.1029/2006JG000365.
- Irvine, J., B. E. Law, and K. A. Hibbard (2007), Postfire carbon pools and fluxes in semiarid ponderosa pine in Central Oregon, *Global Change Biol.*, **13**, 1748–1760.
- Jarvis, P. G., and K. G. McNaughton (1986), Stomatal control of transpiration: Scaling up from leaf to region, *Adv. Ecol. Res.*, **15**, 1–49.
- Jenkins, J. P., A. D. Richardson, B. H. Braswell, S. V. Ollinger, D. Y. Hollinger, and M. L. Smith (2007), Refining light-use efficiency calculations for a deciduous forest canopy using simultaneous tower-based carbon flux and radiometric measurements, *Agr. Forest Meteorol.*, **143**, 64–79.
- Jones, H. G. (1992), *Plants and Microclimate: A Quantitative Approach to Environmental Plant Physiology*, 2nd ed., 428 pp., Cambridge Univ. Press, Cambridge.
- Joyce, R. J., J. E. Nowiak, P. A. Arkin, and P. P. Xie (2004), CMORPH: A method that produces global precipitation estimates from passive microwave and infrared data at high spatial and temporal resolution, *J. Hydrometeorol.*, **5**, 487–503.
- June, T., J. R. Evans, and G. D. Farquhar (2004), A simple new equation for the reversible temperature dependence of photosynthetic electron transport: A study on soybean leaf, *Funct. Plant Biol.*, **31**, 275–283.

- Kalma, J. D., and D. L. B. Jupp (1990), Estimating evaporation from pasture using infrared thermometry - evaluation of a one-layer resistance model, *Agr. Forest Meteorol.*, **51**, 223–246.
- Kalma, J. D., T. R. McVicar, and M. F. McCabe (2008), Estimating land surface evaporation: A review of methods using remotely sensed surface temperature data, *Surv. Geophys.*, **29**, 421–469.
- Kalnay, E., et al. (1996), The NCEP/NCAR 40-year reanalysis project, *Bull. Am. Meteorol. Soc.*, **77**, 437–471.
- Kikuzawa, K. (1995), The basis for variation in leaf longevity of plants, *Vegetatio*, **121**, 89–100.
- Kimball, J. S., M. Zhao, K. C. McDonald, and S. W. Running (2006), Satellite remote sensing of terrestrial net primary production for the pan-Arctic basin and Alaska, *Mitig. Adapt. Strat. Glob. Change*, **11**, 782–804, doi:10.1007/s11027-005-9014-5.
- Kimball, J. S., et al. (2007), Recent climate-driven increases in vegetation productivity for the western Arctic: Evidence for an acceleration of the northern terrestrial carbon cycle, *Earth Interact.*, **11**, 1–30.
- Kistler, R., et al. (2001), The NCEP-NCAR 50-year reanalysis: Monthly means CD-ROM and documentation, *Bull. Am. Meteorol. Soc.*, **82**, 247–267.
- Kobayashi, N., T. Hiyama, Y. Fukushima, M. L. Lopez, T. Hirano, and Y. Fujinuma (2007), Nighttime transpiration observed over a larch forest in Hokkaido, Japan, *Water Resour. Res.*, **43**, W03407, doi:10.1029/2006WR005556.
- Kummerow, C., et al. (2001), The evolution of the Goddard profiling algorithm (GPROF) for rainfall estimation from passive microwave sensors, *J. Appl. Meteorol.*, **40**, 1801–1820.
- Kwon, H. J., W. C. Oechel, R. C. Zulueta, and S. J. Hastings (2006), Effects of climate variability on carbon sequestration among adjacent wet sedge tundra and moist tussock tundra ecosystems, *J. Geophys. Res.*, **111**, G03014, doi:10.1029/2005JG000036.
- Larcher, W. (2003), *Physiological Plant Ecology: Ecophysiology and Stress Physiology of Functional Groups*, 513 pp., Springer-Verlag, Berlin.
- Leuning, R., H. A. Cleugh, S. J. Zegelin, and D. Hughes (2005), Carbon and water fluxes over a temperate Eucalyptus forest and a tropical wet/dry savanna in Australia: Measurements and comparison with MODIS remote sensing estimates, *Agr. Forest Meteorol.*, **129**, 151–173.
- Leuning, R., Y. Q. Zhang, A. Rajaud, H. Cleugh, and K. Tu (2008), A simple surface conductance model to estimate regional evaporation using MODIS leaf area index and the Penman-Monteith equation, *Water Resour. Res.*, **44**, W10419, doi:10.1029/2007WR006562.
- Lhomme, J. P. (1997), A theoretical basis for the Priestley-Taylor coefficient, *Bound.-Layer Meteorol.*, **82**, 179–191.
- Lindroth, A. (2000a), Flakaliden, Sweden, The Euroflux dataset 2000, in *Carbon, Water and Energy Exchanges of European Forests*, edited by R. Valentini, p. 300, Springer-Verlag, Heidelberg.
- Lindroth, A. (2000b), Norunda, Sweden, The Euroflux dataset 2000, in *Carbon, Water and Energy Exchanges of European Forests*, edited by R. Valentini, p. 300, Springer-Verlag, Heidelberg.
- Lipson, D. A., R. F. Wilson, and W. C. Oechel (2005), Effects of elevated atmospheric CO₂ on soil microbial biomass, activity, and diversity in a chaparral ecosystem, *Appl. Environ. Microbiol.*, **71**, 8573–8580.
- Litvak, M., S. Miller, S. C. Wofsy, and M. Goulden (2003), Effect of stand age on whole ecosystem CO₂ exchange in the Canadian boreal forest, *J. Geophys. Res.*, **108**(D3), 8225, doi:10.1029/2001JD000854.
- Livingstone, D. M., and M. T. Dokulil (2001), Eighty years of spatially coherent Austrian lake surface temperatures and their relationship to regional air temperature and the North Atlantic Oscillation, *Limnol. Oceanogr.*, **46**(5), 1220–1227.
- L'vovich, M. I., and G. F. White (1990), Use and transformation of terrestrial water systems, in *The Earth as Transformed by Human Action: Global and Regional Changes in the Biosphere Over the Past 300 Years*, edited by B. L. Turner II et al., pp. 235–252, Cambridge Univ. Press, New York.
- Mazumder, A., W. D. Taylor, D. J. McQueen, and D. R. S. Lean (1990), Effects of fish and plankton on lake temperature and mixing depth, *Science*, **247**, 312–315.
- Meehl, G. A., et al. (2007), Global climate projections, in *Climate Change 2007: The Physical Science Basis*, edited by S. Solomon et al., Cambridge Univ. Press, Cambridge.
- Meyers, T. P., and S. E. Hollinger (2004), An assessment of storage terms in the surface energy balance of maize and soybean, *Agr. Forest Meteorol.*, **125**, 105–115.
- Migliavacca, M., et al. (2009), Seasonal and interannual patterns of carbon and water fluxes of a poplar plantation under peculiar eco-climatic conditions, *Agr. Forest Meteorol.*, **149**, 1460–1476.
- Monson, R. K., et al. (2005), Climatic influences on net ecosystem CO₂ exchange during the transition from wintertime carbon source to springtime carbon sink in a high-elevation, subalpine forest, *Oecologia*, **146**(1), 130–147.
- Monteith, J. L. (1965), Evaporation and environment. The state and movement of water in living organisms, in *Symposium of the Society of Experimental Biology*, pp. 205–234, Cambridge University Press, Cambridge.
- Monteith, J., and M. Unsworth (2007), *Principles of environmental physics*, 418 pp., Academic Press, San Diego, CA.
- Monteith, J. L. (1972), Solar radiation and productivity in tropical ecosystem, *J. Appl. Ecol.*, **9**, 747–766.
- Morrill, J. C., R. C. Bales, and M. H. Conklin (2005), Estimating stream temperature from air temperature: Implications for future water quality, *J. Environ. Eng.-ASCE*, **131**, 139–146.
- Mu, Q., F. A. Heinsch, M. Zhao, and S. W. Running (2007), Development of a global evapotranspiration algorithm based on MODIS and global meteorology data, *Remote Sens. Environ.*, **111**, 519–536.
- Mu, Q., L. A. Jones, J. S. Kimball, K. C. McDonald, and S. W. Running (2009), Satellite assessment of land surface evapotranspiration for the pan-Arctic domain, *Water Resour. Res.*, **45**, W09420, doi:10.1029/2008WR007189.
- Nemani, R. R., and S. W. Running (1989), Estimation of Regional Surface-Resistance to Evapotranspiration from Ndvi and Thermal-IR AVHRR Data, *J. Appl. Meteorol.*, **28**, 276–284.
- Nishida, K., R. R. Nemani, J. M. Glassy, and S. W. Running (2003), Development of an evapotranspiration index from aqua/MODIS for monitoring surface moisture status, *IEEE Trans. Geosci. Remote Sens.*, **41**(2), 493–501.
- Noormets, A., J. Chen, and T. R. Crow (2007), Age-dependent changes in ecosystem carbon fluxes in managed forests in northern Wisconsin, USA, *Ecosystems*, **10**(2), 187–203.
- Norman, J. M., W. P. Kustas, and K. S. Humes (1995), A two-source approach for estimating soil and vegetation energy fluxes from observations of directional radiometric surface temperature, *Agr. Forest Meteorol.*, **77**, 263–293.
- Oechel, W. C., G. L. Vourlieties, S. J. Hastings, R. M. Zulueta, L. D. Hinzman, and D. L. Kane (2000), Acclimation of ecosystem CO₂ exchange in the Alaskan Arctic in response to decadal climatic warming, *Nature*, **406**, 978–981.
- Pan, M., and E. F. Wood (2006), Data assimilation for estimating the terrestrial water budget using a constrained ensemble Kalman filter, *J. Hydrometeorol.*, **7**, 534–547.
- Pejam, M. R., M. A. Arain, and J. H. McCaughey (2006), Energy and water vapour exchanges over a mixedwood boreal forest in Ontario, Canada, *Hydrol. Process.*, **20**, 3709–3724.
- Pilgrim, J. M., X. Fang, and H. G. Stefan (1998), Stream temperature correlations with air temperatures in Minnesota: Implications for climate warming, *J. Am. Water Resour. As.*, **34**, 1109–1121.
- Pinker, R. T., and I. Laszlo (1992), Modeling surface solar irradiance for satellite applications on a global scale, *J. Appl. Meteorol.*, **31**, 194–211.
- Pinzon, J., M. E. Brown, and C. J. Tucker (2005), Satellite time series correction of orbital drift artifacts using empirical mode decomposition, in *Hilbert-Huang Transform: Introduction and Applications*, edited by N. E. Huang and S. S. P. Shen, pp. 167–186, World Scientific Publishing Co. Pte. Ltd., Singapore.
- Powell, T. L., H. L. Gholz, K. L. Clark, G. Starr, W. P. Cropper, and T. A. Martin (2008), Carbon exchange of a mature, naturally regenerated pine forest in north Florida, *Global Change Biol.*, **14**, 2523–2538.
- Priestley, C. H. B., and R. J. Taylor (1972), On the assessment of surface heat flux and evaporation using large-scale parameters, *Mon. Weather Rev.*, **100**, 81–92.
- Reich, P. B., I. J. Wright, and C. H. Lusk (2007), Predicting leaf physiology from simple plant and climate attributes: A global GLOPNET analysis, *Ecol. Appl.*, **17**, 1982–1988.
- Rudolf, B., and U. Schneider (2005), Calculation of gridded precipitation data for the global land-surface using in-situ gauge observations, in *Proceedings of the 2nd Workshop of the International Precipitation Working Group IPWG*, Monterey, October 2004.
- Ryu, Y., D. D. Baldocchi, S. Ma, and T. Hehn (2008), Interannual variability of evapotranspiration and energy exchange over an annual grassland in California, *J. Geophys. Res.*, **113**, D09104, doi:10.1029/2007JD009263.

- Sagerfors, J., A. Lindroth, A. Grelle, L. Klemetsson, P. Weslien, and M. Nilsson (2008), Annual CO₂ exchange between a nutrient-poor, minerotrophic, boreal mire and the atmosphere, *J. Geophys. Res.*, **113**, G01001, doi:10.1029/2006JG000306.
- Schmid, H. P., C. S. B. Grimmer, F. Cropley, B. Offerle, and H. B. Su (2000), Measurements of CO₂ and energy fluxes over a mixed hardwood forest in the mid-western United States, *Agr. Forest Meteorol.*, **103**, 357–374.
- Scott, R. L. (2010), Using watershed water balance to evaluate the accuracy of eddy covariance evaporation measurements for three semiarid ecosystems, *Agr. Forest Meteorol.*, **150**, 219–225.
- Sheffield, J., C. R. Ferguson, T. J. Troy, E. F. Wood, and M. F. McCabe (2009), Closing the terrestrial water budget from satellite remote sensing, *Geophys. Res. Lett.*, **36**, L07403, doi:10.1029/2009GL037338.
- Sorooshian, S., K. L. Hsu, X. Gao, H. V. Gupta, B. Imam, and D. Braithwaite (2000), Evaluation of PERSIANN system satellite-based estimates of tropical rainfall, *Bull. Am. Meteorol. Soc.*, **81**, 2035–2046.
- Stewart, R. B., and W. R. Rouse (1977), Substantiation of Priestley and Taylor Parameter $\alpha=1.26$ for potential evaporation in high latitudes, *J. Appl. Meteorol.*, **16**, 649–650.
- Su, Z. (2002), The Surface Energy Balance System (SEBS) for estimation of turbulent heat fluxes, *Hydrol. Earth Syst. Sci.*, **6**(1), 85–99.
- Su, Z., T. Schmugge, W. P. Kustas, and W. J. Massman (2001), An evaluation of two models for estimation of the roughness height for heat transfer between the land surface and the atmosphere, *J. Appl. Meteorol.*, **40**, 1933–1951.
- Suni, T., et al. (2003), Long-term measurements of surface fluxes above a Scots pine forest in Hyttiala, southern Finland, 1996–2001, *Boreal Environ. Res.*, **8**, 287–301.
- Suyker, A. E., and S. B. Verma (2008), Interannual water vapor and energy exchange in an irrigated maize-based agroecosystem, *Agr. Forest Meteorol.*, **148**, 417–427.
- Suyker, A. E., and S. B. Verma (2009), Evapotranspiration of irrigated and rainfed maize-soybean cropping systems, *Agr. Forest Meteorol.*, **149**, 443–452.
- Takagi, K., et al. (2009), Change in CO₂ balance under a series of forestry activities in a cool-temperate mixed forest with dense undergrowth, *Global Change Biol.*, **15**, 1275–1288.
- Tang, J. W., P. V. Bolstad, and J. G. Martin (2009), Soil carbon fluxes and stocks in a Great Lakes forest chronosequence, *Global Change Biol.*, **15**, 145–155.
- Tang, Q. H., S. Peterson, R. H. Cuenca, Y. Hagimoto, and D. P. Lettenmaier (2009), Satellite-based near-real-time estimation of irrigated crop water consumption, *J. Geophys. Res.*, **114**, D05114, doi:10.1029/2008JD010854.
- Tapley, B. D., S. Bettadpur, M. Watkins, and C. Reigber (2004), The gravity recovery and climate experiment: Mission overview and early results, *Geophys. Res. Lett.*, **31**, L09607, doi:10.1029/2004GL019920.
- Tenunen, J., and E. D. Schulze (2000), Bayreuth, Germany, The Euroflux dataset 2000, in *Carbon, Water and Energy Exchanges of European forests*, edited by R. Valentini, p. 300, Springer-Verlag, Heidelberg.
- Thorgeirsson, H., and J. Gudmundson (2000), Gunnarsholt, Iceland, The Euroflux dataset 2000, in *Carbon, Water and Energy Exchanges of European Forests*, edited by R. Valentini, p. 300, Springer-Verlag, Heidelberg.
- Thornton, P. E. (1998), Regional ecosystem simulation: Combining surface- and satellite-based observations to study linkages between terrestrial energy and mass budgets, Ph.D. Dissertation thesis, 280 pp, The University of Montana, Missoula, MT.
- Trenberth, K. E., et al. (2007), Observations: Surface and atmospheric climate change, in *Climate Change 2007: The Physical Science Basis*, edited by S. Solomon et al., Cambridge Univ. Press, Cambridge.
- Tucker, C. J., J. E. Pinzon, M. E. Brown, D. Slayback, E. W. Pak, R. Mahoney, E. Vermote, and N. Saleous (2005), An extended AVHRR 8 km NDVI data set compatible with MODIS and SPOT vegetation NDVI data, *Int. J. Remote Sens.*, **26**, 4485–4498.
- Twine, T. E., et al. (2000), Correcting eddy-covariance flux underestimates over a grassland, *Agr. Forest Meteorol.*, **103**, 279–300.
- Urbanski, S., et al. (2007), Factors controlling CO₂ exchange on timescales from hourly to decadal at Harvard Forest, *J. Geophys. Res.*, **112**, G02020, doi:10.1029/2006JG000293.
- Valentini, R. (2000), Collelongo, Italy, The Euroflux dataset 2000, in *Carbon, water and energy exchanges of European forests*, edited by R. Valentini, p. 300, Springer-Verlag, Heidelberg.
- Veenendaal, E. M., O. Kolle, and J. Lloyd (2004), Seasonal variation in energy fluxes and carbon dioxide exchange for a broad-leaved semi-arid savanna (Mopane woodland) in Southern Africa, *Global Change Biol.*, **10**, 318–328.
- Wever, L. A., L. B. Flanagan, and P. J. Carlson (2002), Seasonal and inter-annual variation in evapotranspiration, energy balance and surface conductance in a northern temperate grassland, *Agr. Forest Meteorol.*, **112**(1), 31–49.
- Wilson, K., et al. (2002), Energy balance closure at FLUXNET sites, *Agr. Forest Meteorol.*, **113**(1–4), 223–243.
- Wilson, T. B., and T. P. Meyers (2007), Determining vegetation indices from solar and photosynthetically active radiation fluxes, *Agr. Forest Meteorol.*, **144**, 160–179.
- Wood, S. A., J. Beringer, L. B. Hutley, A. D. McGuire, A. Van Dijk, and M. Kilinc (2008), Impacts of fire on forest age and runoff in mountain ash forests, *Funct. Plant Biol.*, **35**, 483–492.
- Wylie, B. K., E. A. Fosnight, T. G. Gilmanov, A. B. Frank, J. A. Morgan, M. R. Haferkamp, and T. P. Meyers (2007), Adaptive data-driven models for estimating carbon fluxes in the Northern Great Plains, *Remote Sens. Environ.*, **106**, 399–413.
- Yang, D., D. Kane, Z. Zhang, D. Legates, and B. Goodison (2005), Bias corrections of long-term (1973–2004) daily precipitation data over the northern regions, *Geophys. Res. Lett.*, **32**, L19501, doi:10.1029/2005GL024057.
- Yuan, W. P., G. S. Zhou, Y. H. Wang, X. Han, and Y. S. Wang (2007), Simulating phenological characteristics of two dominant grass species in a semi-arid steppe ecosystem, *Ecol. Res.*, **22**, 784–791.
- Zhang, K., J. S. Kimball, M. Zhao, W. C. Oechel, J. Cassano, and S. W. Running (2007), Sensitivity of pan-Arctic terrestrial net primary productivity simulations to daily surface meteorology from NCEP-NCAR and ERA-40 reanalysis, *J. Geophys. Res.*, **112**, G01011, doi:10.1029/2006JG000249.
- Zhang, K., J. S. Kimball, E. H. Hogg, M. Zhao, W. C. Oechel, J. J. Cassano, and S. W. Running (2008), Satellite-based model detection of recent climate-driven changes in northern high-latitude vegetation productivity, *J. Geophys. Res.*, **113**, G03033, doi:10.1029/2007JG000621.
- Zhang, K., J. S. Kimball, Q. Mu, L. A. Jones, S. J. Goetz, and S. W. Running (2009), Satellite based analysis of northern ET trends and associated changes in the regional water balance from 1983 to 2005, *J. Hydrol.*, **379**, 92–110, doi:10.1016/j.jhydrol.2009.09.047.
- Zhang, Y. Q., F. H. S. Chiew, L. Zhang, R. Leuning, and H. A. Cleugh (2008), Estimating evaporation and runoff using MODIS leaf area index and the Penman-Monteith equation, *Water Resour. Res.*, **44**, W10420, doi:10.1029/2007WR006563.
- Zhao, L., S. X. Xu, Y. Li, Y. Tang, X. Zhao, S. Gu, M. Du, and G. Yu (2007), Relations between carbon dioxide fluxes and environmental factors of *Kobresia humilis* meadows and *Potentilla fruticosa* meadows, *Front. Biol. China*, **2**, 324–332.
- Zhao, M., S. W. Running, F. A. Heinsch, and R. R. Nemani (2008), Terrestrial primary production from MODIS, in *Land Remote Sensing and Global Environmental Change: NASA's EOS and the Science of ASTER and MODIS*, edited by C. Justice and M. Abrams, pp. 423–444, Springer, New York.

J. S. Kimball and K. Zhang, Flathead Lake Biological Station, University of Montana, 32125 Bio Station Lane, Polson, MT 59860-6815, USA. (zhang@ntsg.umt.edu)

R. R. Nemani, NASA Ames Research Center, Moffett Field, CA 94035, USA.

S. W. Running, Numerical Terradynamic Simulation Group, University of Montana, 32 Campus Drive 1224, Missoula, MT 59812-1224, USA.